remote sensing

MDPI

Article

Performance Evaluation of Inherent Optical Property Algorithms and Identification of Potential Water Quality Indicators Using GCOM-C Data in Eutrophic Lake Kasumigaura, Japan

Misganaw Choto [1], Hiroto Higa [1,*], Salem Ibrahim Salem [2,3], Eko Siswanto [4,5], Takayuki Suzuki [1] and Martin Mäll [1]

[1] Institute of Urban Innovation, Yokohama National University, Hodogaya, Yokohama 240-8501, Kanagawa, Japan; choramo-choto-kb@ynu.jp (M.C.)
[2] Faculty of Engineering, Kyoto University of Advanced Science, 18 Yamanouchi, Gotanda, Ukyo, Kyoto 615-8577, Kyoto, Japan; salem.ibrahim@kuas.ac.jp
[3] Faculty of Engineering, Alexandria University, Lotfy El-Sied St. Off Gamal Abd El-Naser-Alexandria, Alexandria 11432, Egypt
[4] Research Institute for Global Change, Japan Agency for Marine-Earth Science and Technology, Yokohama 236-0001, Kanagawa, Japan; ekosiswanto@jamstec.go.jp
[5] Advanced Institute for Marine Ecosystem Change (WPI-AIMEC), Yokohama 236-0001, Kanagawa, Japan
* Correspondence: higa-h@ynu.ac.jp; Tel.: +81-45-339-4238

Abstract: Lake Kasumigaura, one of Japan's largest lakes, presents significant challenges for remote sensing due to its eutrophic conditions and complex optical properties. Although the Global Change Observation Mission-Climate (GCOM-C)/Second-generation Global Imager (SGLI)-derived inherent optical properties (IOPs) offer water quality monitoring potential, their performance in such turbid inland waters remains inadequately validated. This study evaluated five established IOP retrieval algorithms, including the quasi-analytical algorithm (QAA_V6), Garver–Siegel–Maritorena (GSM), generalized IOP (GIOP-DC), Plymouth Marine Laboratory (PML), and linear matrix inversion (LMI), using measured remote sensing reflectance (*Rrs*) and corresponding IOPs between 2017–2018. The results demonstrated that the QAA had the highest performance for retrieving absorption of particles (a_p) with a Pearson correlation (r) = 0.98, phytoplankton (a_{ph}) with r = 0.97, and non-algal particles (a_{nap}) with r = 0.85. In contrast, the GSM algorithm exhibited the best accuracy for estimating absorption by colored dissolved organic matter (a_{CDOM}), with r = 0.87, along with the lowest mean absolute percentage error (MAPE) and root mean square error (RMSE). Additionally, a strong correlation (r = 0.81) was observed between SGLI satellite-derived remote-sensing reflectance (R_{rs}) and in situ measurements. Notably, a high correlation was observed between the a_{ph} (443 nm) and the chlorophyll a (Chl-a) concentration (r = 0.84), as well as between the backscattering coefficient (b_{bp}) at 443 nm and inorganic suspended solids (r = 0.64), confirming that IOPs are reliable water quality assessment indicators. Furthermore, the use of IOPs as variables for estimating water quality parameters such as Chl-a and suspended solids showed better performance compared to empirical methods.

Keywords: inherent optical properties (IOPs) algorithm; SeaDAS; GCOM-C/SGLI; remote sensing reflectance; water quality

check for updates

Academic Editors: Anita Simic-Milas and Yuhong He

Received: 17 February 2025
Revised: 14 April 2025
Accepted: 24 April 2025
Published: 2 May 2025

Citation: Choto, M.; Higa, H.; Salem, S.I.; Siswanto, E.; Suzuki, T.; Mäll, M. Performance Evaluation of Inherent Optical Property Algorithms and Identification of Potential Water Quality Indicators Using GCOM-C Data in Eutrophic Lake Kasumigaura, Japan. *Remote Sens.* **2025**, *17*, 1621. https://doi.org/10.3390/rs17091621

Copyright: © 2025 by the authors. Licensee MDPI, Basel, Switzerland. This article is an open access article distributed under the terms and conditions of the Creative Commons Attribution (CC BY) license (https://creativecommons.org/licenses/by/4.0/).

1. Introduction

The uneven distribution of lakes and marshes as inland water bodies across the globe leads to notable regional variations in water availability, biodiversity, aquatic ecosystems,

and biogeochemical properties [1,2]. These water bodies play a vital role by contributing to biodiversity, nutrient cycling, environmental stability, supplying drinking water, supporting aquaculture, enabling recreational activities, and offering other vital benefits that contribute to human well-being and the health of global ecosystems [3,4]. However, in environments where primary production is high and water exchange is limited, problems such as organic pollution and eutrophication occur, emphasizing the need for sustainable monitoring and management of water systems to preserve ecological balance [5]. Additionally, numerous studies have highlighted the effects of recent climate change on lake ecosystems [6,7]. Therefore, it is crucial to consistently monitor ecosystem trends and changes in water quality [8–10].

Ocean color remote sensing by satellites provides the means for sustainable environmental monitoring with low labor and cost [11,12]. In recent years, high-resolution spatiotemporal observations by satellites such as the Global Change Observation Mission-Climate (GCOM-C)/Second-generation Global Imager (SGLI), Sentinel-3/Ocean and Land Color Imager (OLCI), and GEO-KOMPSAT-2B/Geostationary Ocean Color Imager-II (GOCI-II) have been realized, enabling detailed spatiotemporal water quality observations even for water bodies such as lakes, which have smaller spatial scales compared to those of marine areas [13–16]. However, as pointed out in many previous studies, optically complex water bodies such as lakes present several challenges, including atmospheric correction and water quality estimation errors [17–19]. These challenges are due to the diverse optical properties of lakes, which are influenced by factors such as depth, types of suspended matter, and the presence of various types of organic and inorganic materials. This has led to extensive research on the development and verification of various atmospheric correction models and water quality estimation models to enhance accuracy and reliability [20,21]. The complexity of lake environments requires specific algorithms that can accurately separate the contributions of different water constituents from the overall optical signal detected by satellites.

The effectiveness of inherent optical properties (IOPs) depends on using well-validated algorithms, particularly in environments such as highly eutrophic and optically complex waters [22]. These algorithms come in various forms and are designed to generate a wide range of optical data products, each serving different purposes [10,23]. Semi-analytical algorithms (SAAs) are essential for deriving IOPs from ocean color data, with widely used methods including the QAA in its various versions (QAA_v5, QAA_v6, QAA710, QAA716, and QAA750E), which employ spectral decomposition to retrieve absorption and backscattering coefficients [10,18,24,25]. GIOP, particularly GIOP-DC, offers a modular framework with customizable parameterizations [10,26,27], improving flexibility but requiring careful sub-model selection [23]. The GSM algorithm uses nonlinear optimization for simultaneous IOP retrieval [28], performing well in open ocean waters but requiring constraints for complex environments [10,27,29]. The PML algorithm is regionally optimized for coastal waters [30], balancing accuracy in moderately turbid conditions. Additionally, linear matrix inversion (LMI) methods provide an alternative by solving radiative transfer equations directly [31,32], offering transparency in IOP separation but being sensitive to noise and initial assumptions. Each algorithm exhibits unique advantages and limitations in satellite-based water quality monitoring, with performance varying significantly across different water types [10,27,29]. Ensuring these IOP algorithms are validated is crucial for generating accurate, reliable, and actionable data and minimizing uncertainty, which supports water quality monitoring, ecosystem management, and the assessment of biogeochemical characteristics [21,23,33]. Accurate in situ IOP measurements are essential for ensuring reliable remote sensing validation, which enhances the ability to estimate critical water quality parameters such as chlorophyll a, suspended

solids, and dissolved organic matter. However, optically complex waters, often rich in phytoplankton, organic material, and non-algal particles, introduce unique challenges for optical measurements [34,35]. By developing and refining strong algorithms, we can significantly improve remote sensing capabilities. This includes tracking harmful algal blooms, monitoring ecosystem health, and adapting tools to fit a wide range of aquatic environments. Ultimately, these developments offer dependable, high-quality data that facilitate informed decision-making and promote sustainable water resource management [36,37].

Many studies on water quality estimations using satellite data have focused on chlorophyll a (Chl-a), suspended particulate matter, and other parameters, while others have focused on estimating IOPs. It has been reported that the IOP approach is effective for understanding biogeochemical dynamics and characterizing the water quality of target water bodies [12,38,39]. The estimation of IOPs from satellite data would make it possible not only to understand the light environment in water bodies, but also to determine optical properties related to particulate and dissolved organic matter (DOM) and particulate inorganic matter [39,40]. This would allow the simultaneous acquisition of multiple water quality parameters from satellite data, contributing to meaningful environmental monitoring. However, IOP estimation is sensitive to atmospheric correction errors since it uses multiple wavelengths of remote sensing reflectance (R_{rs}) captured by satellites, leading to uncertainties in the spatial representation of IOPs [33,41–44]. Additionally, although many IOP estimation algorithms have been proposed, they are often based on empirical methods, semi-analytical inversion methods, and machine learning models, leaving many unknowns regarding their applicability to optically complex water bodies [11,25,26,28,30,32,45]. IOPs provide insights into the absorption and scattering properties of water, which are influenced by substances such as phytoplankton. In the assessment of water quality, they can reveal biogeochemical components such as Chl-a, particulate organic nitrogen (PON), particulate organic carbon (POC), and suspended solids (SS) [46,47]. Chl-a is a key pigment in phytoplankton. It influences the color of water [16,48,49], enabling the estimation of algal biomass and the monitoring of eutrophication through specific wavelength absorption. PON and POC, indicative of organic matter in water, affect both scattering and absorption, providing insights into biogeochemical cycles and nutrient availability [50–54]. SS contribute to increased turbidity, leading to the attenuation of light transmission through the water column and the intensification of backscattering effects. This is primarily caused by the enhanced scattering and absorption of photons by the elevated concentration of particulate matter [55–58].

Remote sensing has been used to explore the optical properties of water bodies across various regions and a wide range of aquatic environments [5,35,41]. Remote sensing provides unparalleled capabilities for synoptic spatial coverage, high temporal resolution, and large-scale applicability in water quality monitoring [59,60], overcoming the inherent limitations of in situ sampling methods. Satellite-derived IOPs offer critical insights into spatial heterogeneity and seasonal dynamics of aquatic ecosystems. This study examines the case of Lake Kasumigaura, the second-largest lake in Japan, which is a vital component of the region's ecosystem, economy, and water resource management system [61]. However, similarly to many freshwater bodies worldwide, it faces significant environmental challenges, including eutrophication, pollution, and water quality deterioration, driven by both anthropogenic activities and natural processes [62]. Furthermore, climatic variations and seasonal hydrodynamics exacerbate water quality issues, complicating management and restoration efforts. Previous research has developed various methods to assess water quality in Lake Kasumigaura, focusing on the application of machine

learning and algorithms to predict Chl-a and suspended solids using remote sensing data [16,63–65]. However, addressing these intricate challenges requires extensive water quality parameters to understand the drivers of water quality changes and to develop effective mitigation strategies for sustainable lake management [66,67].

The aim of this study was to identify suitable IOP algorithms and the key IOP indicators for enhanced water quality monitoring in eutrophic aquatic environments, assuring higher accuracy and minimal errors. Specifically, the study evaluates the performance of five IOP algorithms, each developed with distinct characteristics of optical properties, and to explore the relationship between IOPs and water quality parameters. The research builds on further understanding the light environment in aquatic systems through IOPs and evaluating their potential for estimating water quality parameters. Using measured R_{rs} and IOP data from Lake Kasumigaura, the accuracy of the five IOP algorithms was validated. The study also examined the precision of atmospheric correction and IOP estimation using GCOM-C satellite data. Lastly, the relationship between the estimated IOPs and water quality metrics was analyzed to assess the viability of IOP-based monitoring for water quality evaluation.

2. Materials and Methods

2.1. Study Area

Lake Kasumigaura, the second-largest lake in Japan, is located northeast of Tokyo and has a surface area of 167.63 km^2 (Figure 1). The surrounding area largely consists of natural landscapes and agricultural lands. The lake has experienced notable shifts in phytoplankton communities, nutrient ratios, and water temperature [68,69] and is used for fishing, irrigation, tourism, and recreation [70]. Since 1977, the National Institute for Environmental Studies (NIES) has been conducting regular monthly observations at ten monitoring stations, as shown in Figure 1.

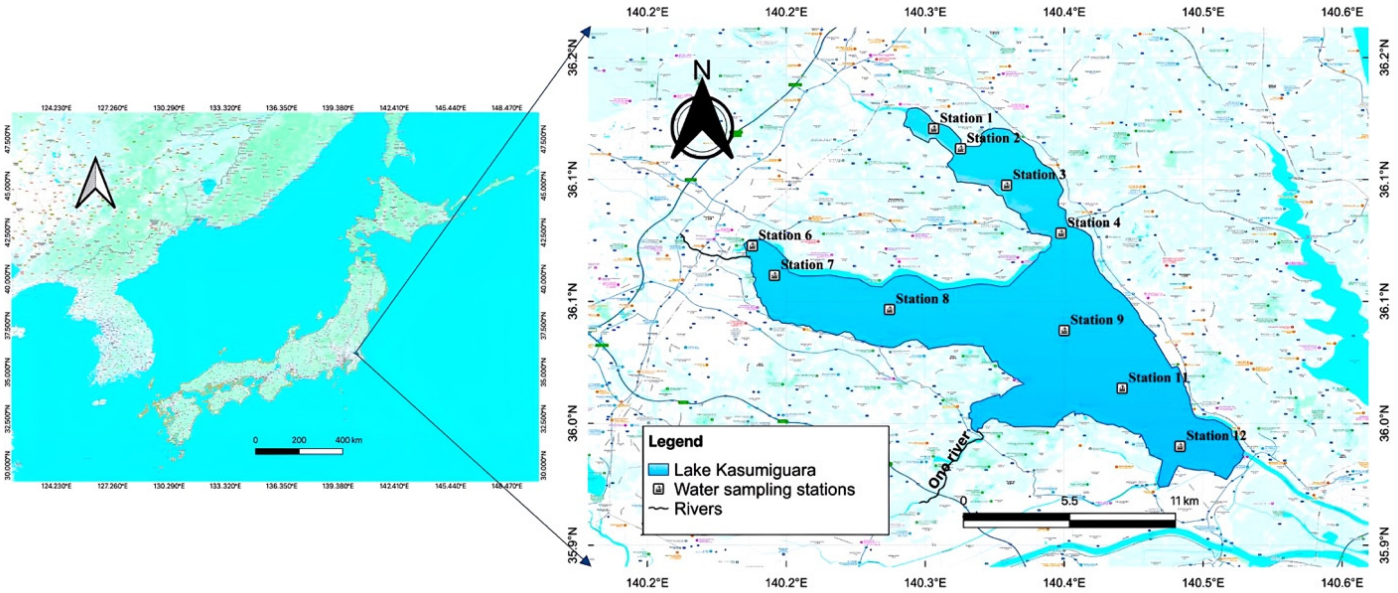


Figure 1. Location of Lake Kasumigaura and water sampling stations.

2.2. Data Collection

2.2.1. Field Observations

Between 2017 and 2018, in situ observations were conducted at ten spatially distributed stations (Figure 1). Sampling was conducted during the optimal season (primarily summer to autumn) to ensure favorable conditions, avoiding periods of extreme weather such as

heavy rain or strong winds that could affect lake water sampling and measurements. Due to this temporal constraint, the validation results may not fully encompass the complete range of seasonal R_{rs} and IOP variations. Optical measurements, including the upward radiance and downward irradiance, were performed at 2 nm intervals using the hyperspectral radiometers TRIOS RAMSES-ARC for radiance and RAMSES-ACC for irradiance [71]. For the measurement of backscattering (b_b), HOBI Labs HydroScat was used to measure the total b_b by applying a σ correction to correct for the effect of light dissipation at the optical path length between the sensors (HOBI-Labs_Inc., Tucson, AZ, USA) [72,73]. For the measurement of optical absorption coefficients, collected surface water was used and filtered through a Whatman Nuclepore membrane (pore size: 0.4 µm). The filtrate was placed in a 10 cm quartz cell, and absorption of colored dissolved organic matter (a_y) was measured using a Shimadzu MPS-2400 spectrophotometer (Shimadzu Corporation, Kyoto, Japan) [74]. In situ optical ground data were obtained by collecting lake water samples from designated stations, filtering them through 25 mm glass microfiber filters (Whatman glass microfiber filters grade GF/F: 0.7 µm), and mounting them on a spectrophotometer (Shimadzu UV-2400). The optical absorption coefficient (a_p) of the particles was measured using a spectrophotometer (Shimadzu MPS-2400) equipped with an end-on photomultiplier for detecting light intensity across a specified wavelength range, allowing for precise quantification of particle absorption and scattering properties [75]. The optical absorption coefficient of tryptone (detritus + inorganic suspended matter) was then measured by immersing the filtered Whatman glass microfiber filters in ethanol on a filter funnel to confirm that the phytoplankton pigment had been removed, and then the optical absorption coefficient was measured again; a_{ph} was then calculated by subtracting the optical absorption coefficient of tryptone from the a_p [76,77]. The IOPs, namely, the $a_p(\lambda)$, $a_{dg}(\lambda)$, $a_{ph}(\lambda)$, and $b_{bp}(\lambda)$, were also derived using the IOP algorithm. According to Yamashita [78], the $a_{dg}(\lambda)$ component, which integrates $a_{CDOM}(\lambda)$ and $a_{NAP}(\lambda)$, can be separated using coefficients derived from least squares regression with the measured $a_{CDOM}(\lambda)$ and derived $a_{dg}(\lambda)$.

2.2.2. Water Quality Dataset by the NIES

The NIES initiated a monitoring project at Lake Kasumigaura in 1977. Since then, it has consistently tracked the lake's water quality and biological characteristics at ten monitoring stations [16,61,66,79,80]. The in-situ water quality data collected by the NIES at Lake Kasumigaura were obtained from monitoring database (accessible at: https://db.cger.nies.go.jp/gem/moni-e/inter/GEMS/database/kasumi/data/water/wq_data.zip; accessed on 2 September 2024). The water quality parameters employed in this study were Chl-a, POC, PON, DON, and SS for the period from 2018 to 2022 [81]. SS collected by the NIES include organic and inorganic SS. To understand the relationship between IOPs and SS, the separation of organic and inorganic SS is important since the ecological role SS play in water bodies depends on whether they are mostly organic or inorganic compounds [82,83]. Organic SS are directly related to the nitrogen content in phytoplankton. Organic and inorganic SS were separated based on the Redfield ratio [84]. The Redfield ratio is the C:N:P ratio of the elemental composition $(CH_2O)_x(NH_3)_y(H_3PO_4)_z$ of marine phytoplankton, which is approximately 106:16:1 [85]. The correlation of IOPs with both organic and inorganic SS was evaluated. The differentiation between organic SS and inorganic SS was critical to accurately assess their respective biological influences on IOPs. The separation of organic SS and inorganic SS enables a more precise evaluation of their individual contributions to light absorption and scattering processes [86].

2.2.3. GCOM-C Satellite Imagery

GCOM-C/SGLI provides multispectral and multi-polarization imagery over a wide range of wavelengths (ultraviolet to infrared). For this study, we acquired GCOM-C/SGLI satellite imagery with a spatial resolution of 250 m, focusing on normalized water-leaving radiance, to estimate R_{rs} over various aquatic systems for the period from 2018 to 2022. R_{rs} serves as the fundamental optical parameter that relates water-leaving radiance to the IOPs of aquatic systems. R_{rs} can be acquired through either in situ measurements or satellite remote sensing [87]. The spectral distribution of $R_{rs}(\lambda)$ is determined by radiometrically measuring the upwelling radiance and downwelling irradiance above the water surface [87,88]. The R_{rs} is defined by the following equation:

$$R_{rs}(\lambda,\ \theta_0,\ \theta,\ \Delta\varnothing) \equiv \frac{L_w(\lambda,\ \theta_0,\ \theta,\ \Delta\varnothing)}{E_d(0^+,\ \lambda,\ \theta_0)}[sr^{-1}] \quad (1)$$

where R_{rs} is the remote sensing reflectance; L_w represents the radiance exiting the water under idealized conditions normalized for the mean Earth–Sun distance, with the Sun at zenith and no atmospheric attenuation; and E_d at 0^+ is the actual solar irradiance reaching the sea surface after accounting for atmospheric absorption and scattering from the top of the atmosphere [89]. Data acquisition involved accessing the Japan Aerospace Exploration Agency's (JAXA) G-Portal system (https://gportal.jaxa.jp/gpr/), where processed level 2 products relevant to water quality monitoring were selected based on our study area's location and acquisition time.

This study utilized level 2 SGLI products with version 3 atmospheric correction processed through an algorithm developed based on the SeaWiFS and MODIS (Gordon and Wang, 1994) approaches [89,90], while incorporating developments from Japanese ocean color satellites ADEOS/OCTS [91] and ADEOS2/GLI [92]. The algorithm implements a sequential correction approach, first removing Rayleigh-scattered radiance from top-of-atmosphere reflectance before addressing the more complex aerosol reflectance component [19,93]. A critical innovation involves the use of dual near-infrared bands coupled with the linear combination index method, which significantly improves water-leaving reflectance estimation in turbid waters by focusing on the NIR band analysis [89]. Further refinements include improved atmospheric transmittance calculations derived directly from these simulations, sophisticated sun glint correction incorporating inter-band parallax compensation, and an automated quality control mechanism that prevents negative water-leaving reflectance through iterative aerosol model reselection [93,94]. This study utilized data from the visible and near-infrared radiometer (SGLI-VNR) and the non-polarization channels, as detailed in Table 1.

Table 1. Center wavelengths and bandwidths of the GCOM-C/SGLI.

Channel	Center Wavelength (nm)	Bandwidth (nm)
VN1	380	10
VN2	412	10
VN3	443	10
VN4	490	10
VN5	530	20
VN6	565	20
VN7	673.5	20
VN8	673.5	20
VN9	763	12
VN10	868.5	20
VN11	868.5	20

2.3. Study Design

The study was structured into two phases to achieve its objectives (Figure 2). In the first phase, the performance of various IOP algorithms was evaluated to identify the best-performing algorithm for each IOP, utilizing measured IOPs (dashed box in Figure 2). In the second phase, the focus was on identifying the key water quality indicators by analyzing the correlation matrix, with an emphasis on parameters showing strong correlations.

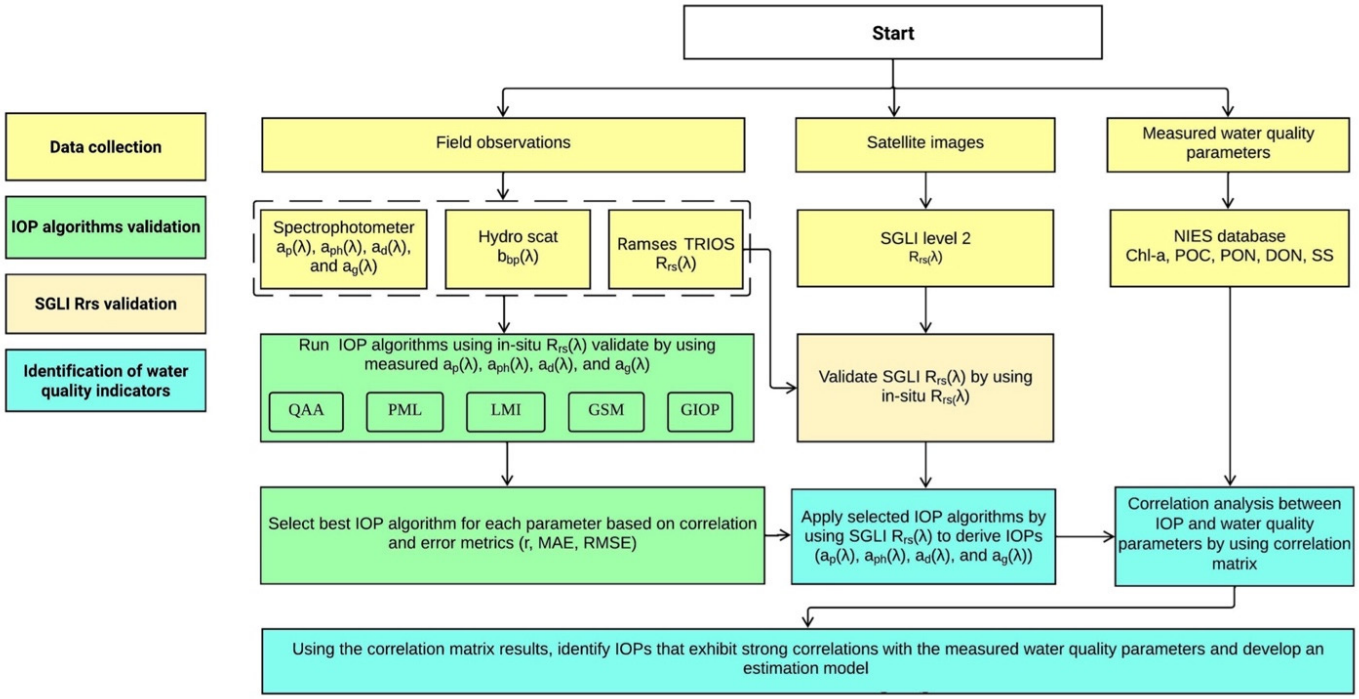


Figure 2. Flowchart illustrating step-by-step processes used in the study. The main components include data collection, methodology development, analysis, and conclusion.

2.4. Semi-Analytical IOP Algorithms

In this study, five IOP algorithms were examined, namely, the quasi-analytical algorithm (QAA), the Graver–Siegel–Maritorena (GSM) algorithm, the generalized IOP (GIOP) algorithm, linear matrix inversion (LMI), and the Plymouth Marine Laboratory (PML) algorithm (Figure 2). Several methods have been developed to retrieve IOPs. Gordon et al. [95] derived the relationship between inherent and apparent optical properties through an analysis of the radiance transfer theory. Hoge and Lyon [32] obtained IOPs using the LMI of oceanic radiance models, with a focus on the analysis of errors from both the model and radiance measurements. The LMI approach utilizes a matrix equation for accurately obtaining IOPs and provides a comprehensive framework for water quality assessment based on R_{rs} [96,97]. The updated MATLAB code for linear matrix inversion, found on the University of Maine website, was downloaded from the IOCCG working group website (http://www.ioccg.org/groups/Software_OCA/Chapter_08_insitu.zip) and modified for SGLI-observed wavelengths before applying IOP inversion. This study applied both in situ data inversion for IOP validation and synthetic data inversion for GCOM-C satellite images. PML IOP inversion models use field-measured data and R_{rs} from satellite images. The PML IOP algorithm's Python code, provided by the IOCCG working group (http://www.ioccg.org/groups/Software_OCA/PML.zip), was modified to apply to the GCOM-C/SGLI satellite images for IOP inversion. The PML algorithm was developed based on the Graver and Siegel nonlinear statistical method based on the ratio between upwelling and downwelling radiance to water reflectance [30]. In this study,

the commonly applied techniques included the utilization of Python (version 3.12) scripts, MATLAB (Release R2023b, Version 23.2) code, and the sea-viewing data analysis system (SeaDAS) software package. SeaDAS version 8.4 was downloaded from the NASA Ocean Color website (https://seadas.gsfc.nasa.gov) and applied to derive IOPs using in situ as well as satellite imagery [12]. Semi-analytical algorithms (SAA) have been developed based on empiricism and the radiative transfer theory [98]. The SeaDAS software, which incorporates semi-analytical algorithms such as the QAA, GIOP algorithm, and GSM algorithm, is commonly used for analyzing marine IOPs derived from ocean color data acquired via satellites [99,100]. In SeaDAS, parameter configurations for IOP retrieval algorithms were were performed by choosing the IOP algorithm version (QAA_v6, GSM, GIOP-DC), defining reference wavelengths, and setting initial constraints for absorption (a_{ph}, a_{dg}) and backscattering (b_{bp}). For QAA_v6, the backscattering slope (η) was raised to 1.0–1.3 to better model high particle loads, while GSM requires modified initial guesses, including an a_{dg} slope (S_{dg}) of 0.0206 nm^{-1} (up from 0.018 nm^{-1}) and a particulate backscattering ratio increased to 1.5 paired with nonlinear optimization. GIOP enables the configuration of spectral constraints and initial estimates for phytoplankton, CDOM, and detritus absorption [26,27]. These settings allow flexible tuning of phytoplankton absorption, CDOM (S_{dg} adjustable from 0.015 to 0.018 nm^{-1}), and backscattering slope (η elevated to 1.2 in eutrophic cases), ensuring accurate retrievals in complex scattering environments. SeaDAS enables the dynamic creation of various semi-analytical algorithms, allowing for the assessment of specific modeling assumptions and the customization of semi-analytical algorithms for given applications [45]. Moreover, the software supports ensemble inversion modeling, which aids in extracting detailed information on absorption and backscattering coefficients derived from ocean color data acquired via satellites [21].

2.5. Accuracy Assessment of Inherent Optical Property Algorithms Using In Situ and Remote Sensing Data

Assessing the accuracy of prediction models is crucial for evaluating their performance [101]. The metrics used in this study are the mean absolute percentage error (MAPE), root mean square error (RMSE), and the sample Pearson correlation coefficient (r). The MAPE and RMSE assess the magnitude of prediction errors, and the sample Pearson correlation coefficient assesses the linear relationship between the predicted and actual values [102].

$$\mathrm{MAPE} = \frac{1}{n}\sum_{i=1}^{n}\left|\frac{x_i - y_i}{x_i}\right| \times 100\% \quad (2)$$

$$\mathrm{RMSE} = \sqrt{\frac{1}{n}\sum_{i=1}^{n}(x_i - y_i)^2 r} \quad (3)$$

$$r = \frac{\sum_{i=1}^{n}(X_i - \bar{x})(Y_i - \bar{Y})}{\sqrt{\sum_{i=1}^{n}(X_i - \bar{x})^2 \sum_{i=1}^{n}(Y_i - \bar{Y})^2}} \quad (4)$$

where n is the number of observations, x_i represents the in situ measured IOPs of the n^{th} observation, and y_i represents the derived IOP value of the i^{th} observation. $\bar{x}$ and $\bar{Y}$ are the means of the in situ measured values and the derived values, respectively. The correlation coefficient was used to understand the relationship of IOPs and the measured water quality parameters using a correlation matrix (heat map) generated for graphical representation [103].

The consistency and dispersion of the comparison between datasets of $a_p(\lambda)$, $a_{ph}(\lambda)$, and $a_{dg}(\lambda)$ derived using the QAA, GIOP, GSM, PML, and LMI IOP algorithms with the measured IOPs (Table 2) were compared using Taylor diagrams. Taylor diagrams are used to characterize the potential of an algorithm in estimating IOPs in terms of the correlation

coefficient, normalized standard deviation, and normalized unit root mean square deviation (uRMSD). In this diagram, a model performs better if the obtained IOPs are closer to the in situ data [104], where in the ideal case, r is equal to one, the normalized uRMSD is zero, and the normalized standard deviation is one [29,105]. The following equation was used to calculate the uRMSD:

$$\text{uRMSD} = \sqrt{\frac{1}{n}\sum_{i=1}^{n}(X_i - Y_i)^2 - \text{Bias}^2} \quad (5)$$

where X_i represents the in situ measured IOP values, Y_i represents the derived IOP values, n is the number of observations, and Bias is the average difference between the derived and in situ measured values.

$$F = \frac{\text{Mean square between (MSB)}}{\text{Mean square within (MSW)}} \quad (6)$$

$$\text{MSB} = \frac{\text{SSB}}{\text{df}_{\text{between}}} \quad (7)$$

$$\text{MSB} = \frac{\text{SSW}}{\text{df}_{\text{within}}} \quad (8)$$

$$p - \text{value} = P\left(F_{\text{calculated}} \geq F_{\text{critical}} \middle| d_{f1}, d_{f2}\right) \quad (9)$$

The F-statistic ($F_{\text{calculated}}$) compares the variation between groups (SSB) to the variation within groups (SSW). The degrees of freedom for the numerator (d_{f1}) are $k - 1$, for the denominator (d_{f2})—$N - k$. The F_{critical} value from the F-distribution at the significance level (α) determines if the F-statistic is significant.

Table 2. Descriptive statistics of the measured IOPs $a_p(\lambda)$, $a_{ph}(\lambda)$, $a_{NAP}(\lambda)$, and $a_{CDOM}(\lambda)$ of the observed SGLI wavelengths in Lake Kasumigaura [unit: m^{-1}]. SD denotes standard deviation.

Measured IOP	Sample Size	Min	Max	Mean	Median	SD
a_p (412 nm)	24	0.93	1.97	1.63	1.69	0.34
a_p (443 nm)	24	0.76	1.90	1.30	1.25	0.30
a_p (490 nm)	24	0.41	1.14	0.74	0.71	0.19
a_p (530 nm)	24	0.23	0.58	0.41	0.40	0.09
a_p (565 nm)	24	0.16	0.40	0.28	0.27	0.06
a_p (670 nm)	24	0.22	0.73	0.39	0.33	0.15
a_{ph} (412 nm)	24	0.28	0.99	0.57	0.51	0.23
a_{ph} (443 nm)	24	0.26	1.25	0.57	0.48	0.29
a_{ph} (490 nm)	24	0.12	0.69	0.31	0.25	0.19
a_{ph} (530 nm)	24	0.04	0.37	0.14	0.11	0.09
a_{ph} (565 nm)	24	0.01	0.24	0.08	0.06	0.06
a_{ph} (670 nm)	24	0.16	0.63	0.30	0.25	0.14
a_{NAP} (412 nm)	24	0.075	2.164	1.180	1.512	0.793
a_{NAP} (443 nm)	24	0.049	1.489	0.796	1.036	0.533
a_{NAP} (490 nm)	24	0.031	0.967	0.506	0.637	0.342
a_{NAP} (530 nm)	24	0.018	0.798	0.385	0.457	0.273
a_{NAP} (565 nm)	24	0.013	0.729	0.309	0.345	0.230
a_{NAP} (670 nm)	24	0.0002	0.606	0.203	0.215	0.173
a_{CDOM} (412 nm)	24	0.593	1.548	1.088	1.114	0.288
a_{CDOM} (443 nm)	24	0.429	1.109	0.757	0.785	0.192
a_{CDOM} (490 nm)	24	0.255	0.621	0.442	0.462	0.111
a_{CDOM} (530 nm)	24	0.165	0.377	0.279	0.293	0.067
a_{CDOM} (565 nm)	24	0.121	0.282	0.195	0.204	0.045
a_{CDOM} (670 nm)	24	0.049	0.204	0.083	0.080	0.031

3. Results

3.1. Comparative Analysis of IOP Algorithms

To assess the performance of the IOP algorithms and determine the most suitable algorithm for Lake Kasumigaura, the correlation between the derived and measured IOPs was analyzed across six wavelength bands (412, 443, 490, 530, 565, and 670 nm). These wavelengths were chosen due to their availability in remote sensing satellite imagery and their compatibility with commonly used ocean color sensors (see Table 3) [29].

Table 3. Accuracy assessment results for QAA, PML, LMI, GSM, and GIOP algorithms using in situ measured $a_p(\lambda)$, $a_{ph}(\lambda)$, $a_{NAP}(\lambda)$, and $a_{CDOM}(\lambda)$.

IOP Algorithm	Error Metrics	QAA	PML	LMI	GSM	GIOP
a_p (λ)	MAPE	0.31	0.35	0.36	0.54	0.29
	RMSE	0.29	0.31	0.42	0.57	0.33
	r	0.98	0.96	0.95	0.94	0.95
	F	180.95	139.17	259.35	318.18	169.11
	p-value	8.9×10^{-59}	4.2×10^{-52}	2.6×10^{-68}	6.9×10^{-74}	4.9×10^{-57}
	% between ±30% to 1:1	91.81	85.83	79.31	75.04	85.97
a_{ph} (λ)	MAPE	0.23	0.60	0.56	0.90	0.40
	RMSE	0.08	0.24	0.17	0.21	0.14
	r	0.97	0.69	0.83	0.75	0.88
	F	43.84	30.59	47.49	61.19	37.06
	p-value	6.8×10^{-27}	7.6×10^{-21}	2.3×10^{-28}	2.4×10^{-33}	6.0×10^{-24}
	% between ±30% to 1:1	89.17	56.11	63.89	65.83	75.17
a_{NAP} (λ)	MAPE	2.18	3.10	1.29	0.98	4.02
	RMSE	0.31	0.35	0.34	0.30	0.38
	r	0.85	0.74	0.73	0.84	0.73
	F	103.75	85.76	95.52	147.51	70.39
	p-value	5.5×10^{-45}	1.3×10^{-40}	4.7×10^{-43}	1.5×10^{-53}	2.9×10^{-36}
	% between ±30% to 1:1	74.19	69.58	61.25	75.53	62.03
a_{CDOM} (λ)	MAPE	0.70	0.10	0.52	0.46	0.76
	RMSE	0.23	0.31	0.25	0.21	0.27
	r	0.85	0.65	0.83	0.87	0.79
	F	117.65	60.61	96.28	128.01	84.23
	p-value	5.6×10^{-48}	3.8×10^{-33}	3.1×10^{-43}	4.9×10^{-50}	3.4×10^{-40}
	% between ±30% to 1:1	71.25	52.50	66.67	73.33	59.56

A one-way ANOVA test was conducted to evaluate the performance of five different IOP algorithms, using a sample size of 144 from six bands for each IOP. At a 95% confidence level ($\alpha = 0.05$), the F-critical value, based on the degrees of freedom (4, 138), was approximately 3.89. All the IOP algorithms demonstrated statistically significant differences because their F-values exceeded the F-critical value, with the corresponding *p*-values below 0.0001. In addition to the ANOVA test, correlation coefficients and error metrics were calculated to assess the relationship between the measured and derived IOPs. The results revealed variability in both correlation and error metrics, indicating substantial differences in IOP inversion across the algorithms.

The QAA demonstrated superior performance, with consistently high *r* indicating a strong correlation between the derived and measured values. For $a_p(\lambda)$, it achieved the highest correlation ($r = 0.98$), the lowest errors (MAPE = 0.31, RMSE = 0.29), and an outstanding 91.81% of the values were within ±30% of the 1:1 line. The F-statistic for the QAA was the highest (F = 180.95), reinforcing its robust performance and statistical

significance, with a p-value of 8.9×10^{-59}. Similarly, for $a_{ph}(\lambda)$, the QAA maintained its top performance with r = 0.97, MAPE = 0.23, and RMSE = 0.08. It also achieved a high F-statistic (F = 43.84) and a p-value of 6.8×10^{-27}, signifying strong statistical significance. In terms of accuracy, it was highly reliable, with 89.17% of values within ±30% of the 1:1 line. For $a_{NAP}(\lambda)$, the QAA's performance remained solid with r = 0.85 and an F-statistic of 103.75, highlighting its reliability in this parameter. For $a_{CDOM}(\lambda)$, GSM emerged as the best algorithm, achieving the highest correlation (r = 0.87) and an F-statistic of 128.01. It demonstrated the lowest errors (MAPE = 0.46, RMSE = 0.21), and 73.33% of values were within ±30% of the 1:1 line. The statistical significance of GSM was notable, with a p-value of 4.9×10^{-50}, making it particularly effective for environments dominated by dissolved organic matter. Previous research has shown that the QAA and GSM work well in waters with varying aquatic environmental conditions [10,27].

The GIOP, LMI, and PML algorithms exhibited moderate-to-lower performances across most IOPs. For $a_p(\lambda)$, GIOP achieved r = 0.95 with a reasonable accuracy, though its F-statistic (F = 169.11) and p-value (4.9×10^{-57}) suggested a moderate correlation, still statistically significant but not as strong as the QAA's. For $a_{ph}(\lambda)$, GIOP showed a balanced performance with r = 0.88, MAPE = 0.40, and RMSE = 0.14, but its F-statistic (F = 37.06) indicated a less optimal fit compared to the QAA. GSM performed moderately for most IOPs but excelled in $a_{CDOM}(\lambda)$, reinforcing its performance for dissolved organic matter analysis. The LMI and PML algorithms demonstrated inconsistent and moderate performance results across the IOPs; LMI exhibited moderate-to-high correlations (r = 0.73 to 0.83), but its overall performance remained lower compared to the QAA and GSM. In contrast, the PML algorithm consistently exhibited the lowest performance across the parameters. For $a_{ph}(\lambda)$, PML had the weakest correlation (r = 0.69) and the highest errors (MAPE = 0.60, RMSE = 0.24), with only 56.11% of values within ±30% of the 1:1 line. Its F-statistic of 85.76 and p-value of 1.3×10^{-40} further highlighted its limitations. Similarly, for $a_{CDOM}(\lambda)$, PML's r = 0.65, along with higher errors (MAPE = 1.10, RMSE = 0.31), suggested its limited applicability for accurate IOP inversion in complex aquatic environments, despite its potential use in simpler cases.

The evaluation of the IOP algorithm performance (Table 3 and Figure 3) for total absorption indicates that the QAA had the highest accuracy, followed by the GIOP algorithm. The LMI algorithm showed moderate reliability, whereas the GSM and PML algorithms had low effectiveness, with the PML algorithm having the worst performance. For a_{ph}, the algorithm performance followed the order QAA > GIOP > LMI > GSM > PML. The QAA had the highest accuracy, with the GIOP algorithm closely trailing. The LMI algorithm outperformed the GSM and PML algorithms, which showed the lowest effectiveness for this parameter. Regarding a_{NAP}, the ranking was QAA > GSM > PML > LMI > GIOP. The QAA had the best performance, followed by the GSM algorithm. The PML algorithm outperformed the LMI and GIOP algorithms, which ranked the lowest in this category. For a_{CDOM}, the ranking was GSM > QAA > LMI > GIOP > PML. The GSM algorithm had the best performance, followed by the QAA. However, the QAA had consistently low errors for a_{CDOM} and across all wavelengths, comparable to those of the GSM algorithm. Notably, the LMI algorithm outperformed both the GIOP and PML algorithms, which exhibited the lowest accuracy. Overall, the QAA was the most reliable algorithm, with higher correlation coefficients across all wavelengths for $a_p(\lambda)$, $a_{ph}(\lambda)$, and $a_{NAP}(\lambda)$ and low MAPE and RMSE values for a_{CDOM}. For a_{CDOM}, GSM had the highest correlation, followed by the QAA. The QAA and the GSM algorithms were the most reliable algorithms for IOP estimation at Lake Kasumigaura, offering robust and consistent results with minimal errors across all wavelengths and IOPs. The GIOP algorithm performed well but was slightly less effective. The LMI algorithm exhibited variable performance, often surpassing the PML algorithm, which generally showed lower accuracy.

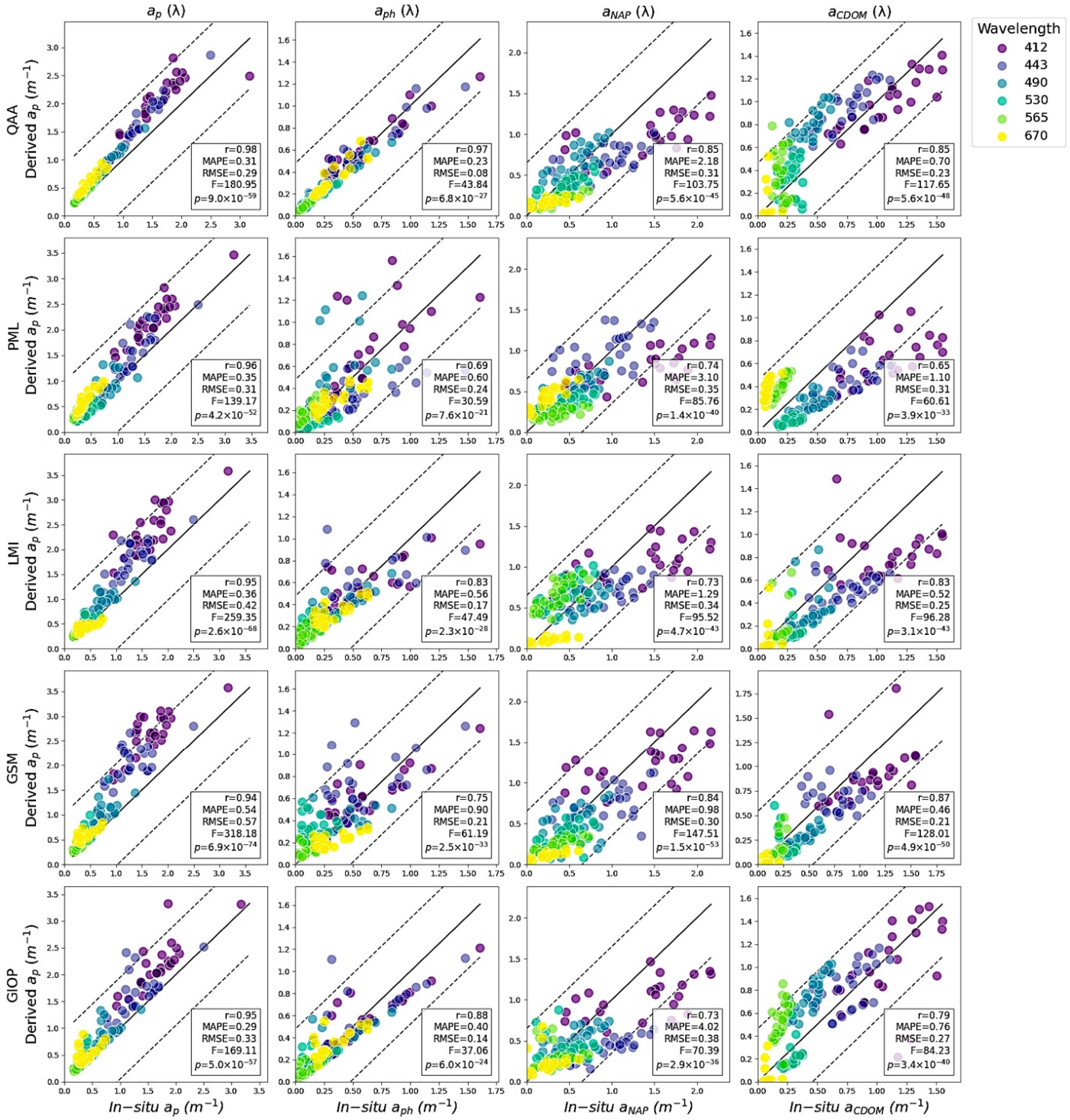


Figure 3. Comparison of a_p (λ), a_{ph}(λ), a_{NAP}(λ), and a_{CDOM}(λ) derived from the IOP algorithms (QAA, PML, LMI, GIOP, GSM) at the observed SGLI wavelengths and the IOPs measured in situ. The black line is 1:1, and the dotted lines are ±30% of the correlation.

The variability in algorithm performance across wavelengths and IOPs highlights the sensitivity of IOP algorithms (Figures 3 and 4). The Taylor diagram results reveal distinct spectral and algorithmic dependencies in the performance of IOP retrievals (Figure 4). The QAA demonstrated strong consistency across most wavelengths (412–670 nm), effectively retrieving a_p, a_{ph}, and a_{CDOM} at shorter wavelengths (412–443 nm), with a shift to a_{NAP} at longer wavelengths (490–670 nm). PML exhibited variable performance, excelling in a_{ph} and a_{NAP} retrievals at mid-range wavelengths (443–565 nm), while GSM and LMI showed

selective accuracy in a_{CDOM} retrievals (490 nm for GSM; 530 nm for LMI). In contrast, GIOP consistently underperformed for a_{NAP} (412 nm) and a_{CDOM} (565 nm), and LMI displayed limitations in a_{CDOM} retrieval at 443 nm and 670 nm. These patterns underscore wavelength-specific algorithm biases, with the QAA exhibiting the broadest spectral versatility, while specialized algorithms (GSM, LMI) performed well only for specific IOPs within narrow spectral ranges. At 670 nm, the smaller deviations suggest measurements that were more consistent, with non-algal particles dominating absorption. Correlation coefficients $r \geq 0.79$ show moderate-to-strong alignment between the predicted and observed values, especially for the QAA. However, the lower correlation values at 530 and 565 nm suggest that these wavelengths were more challenging for the models, likely due to the interplay of particles and absorption phenomena. The QAA performed reliably at 412 to 565 nm, especially in capturing a_{ph}. The GIOP and LMI algorithms had the lowest correlation at 412 and 490 nm for a_{NAP}, and the QAA showed a moderate performance at 670 nm for a_{CDOM}, with r = 0.81 and RMSE = 0.32. The performance of the PML and LMI algorithms generally showed more variability across different types of absorption and wavelengths, with neither method consistently outperforming the others in all scenarios. The low standard deviation of the PML algorithm at 530 nm for $a_{ph}(\lambda)$ suggests low variability in its estimates and indicates a reliable performance. The discrepancies between algorithms at various wavelengths indicate that some are better suited for IOPs, necessitating careful selection based on the intended application. Selecting an algorithm that matches the environmental conditions and optical complexities of the water body under study is essential.

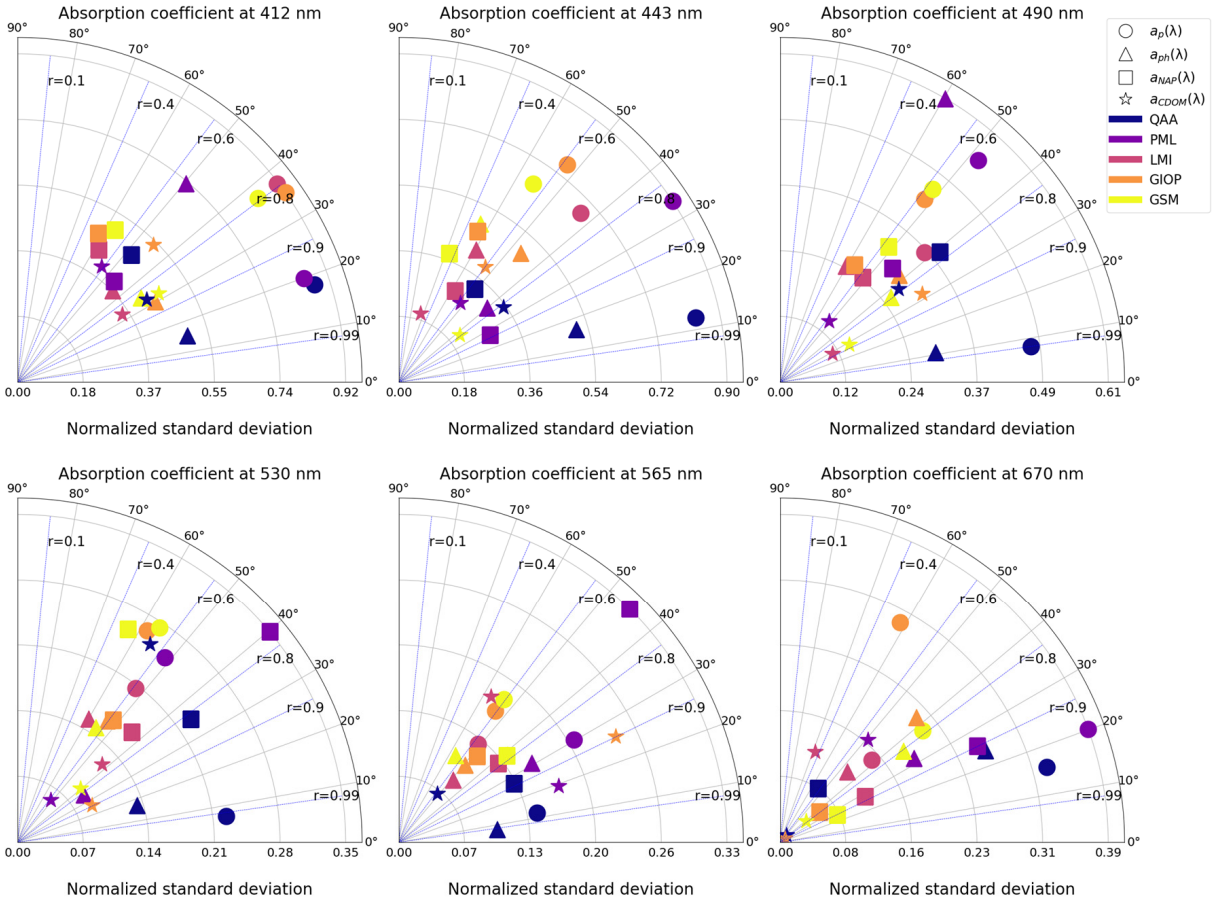


Figure 4. Taylor diagrams showing correlations between the in situ and estimated total a_p, a_{ph}, a_{NAP} and a_{CDOM} at wavelengths of 412, 443, 490, 530, 565, and 670 nm.

3.2. Accuracy Assessment of the GCOM-C/SGLI Satellite Imagery and In Situ Remote Sensing Reflectance

This study conducted an accuracy assessment by acquiring in situ R_{rs} data at ten stations. R_{rs} values were extracted from the level 2 GCOM-C/SGLI satellite images at these locations. The subsequent analysis aimed to evaluate the spectral shape and accuracy of satellite-derived R_{rs} data to determine their applicability for assessing IOPs.

The R_{rs} results in Figure 5a,b exhibited a spectral shape characteristic of organically polluted waters, with prominent light absorption in the blue region. R_{rs} values increased progressively from the blue (443 nm) to green (565 nm) wavelengths, followed by a decrease into the red spectral region (670 nm). The measured R_{rs} spectra demonstrated greater consistency, whereas satellite-derived R_{rs} displayed variability across stations. This pattern aligns with the R_{rs} observations reported by Salem et al. [106].

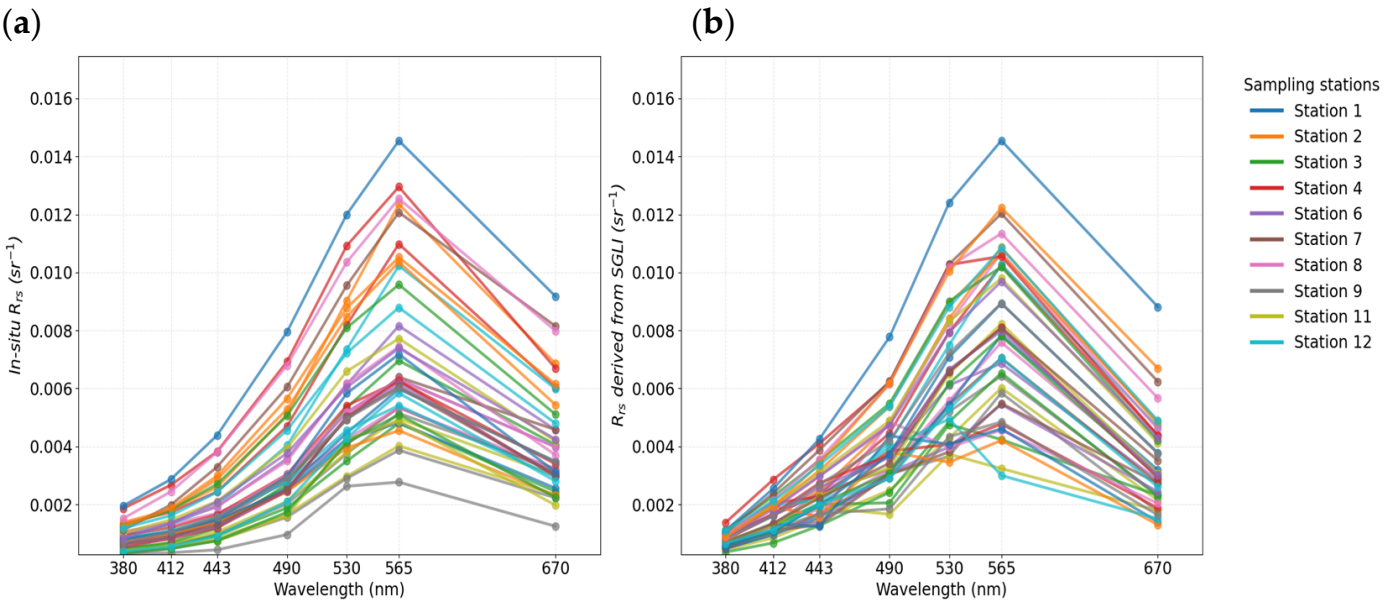


Figure 5. Comparison of R_{rs} spectra at the observed wavelengths of the SGLI: (**a**) in situ R_{rs} collected at 10 sampling stations in Lake Kasumigaura and (**b**) corresponding satellite-derived R_{rs} from the level 2 GCOM-C/SGLI products at coincident locations.

Comparing the in situ measured R_{rs} and the SGLI satellite-derived R_{rs} across the observed wavelengths of the SGLI provides insights into the reliability of satellite observations. Figure 5a,b demonstrates that the spectral shapes of R_{rs} were generally consistent between the two datasets, while Figure 6 further quantified this agreement through a scatter plot comparison of R_{rs} values at each observation wavelength. The correlation coefficients were relatively high across all wavelengths, ranging from 0.81 to 0.91, indicating strong relationships in the R_{rs} spectra. The SGLI-derived R_{rs} exhibited strong spectral agreement with in situ measurements, showing significantly higher correlation coefficients at 490 nm (r = 0.91) and 530 nm (r = 0.89) compared to shorter wavelengths. The MAPE values showed more variation, ranging from 22.4% to 55.0%. The SGLI-derived R_{rs} at 412 nm and 443 nm exhibited a slight overestimation, with MAPE of 50.7% and 55.0%, respectively, indicating moderate deviations from in situ R_{rs}.

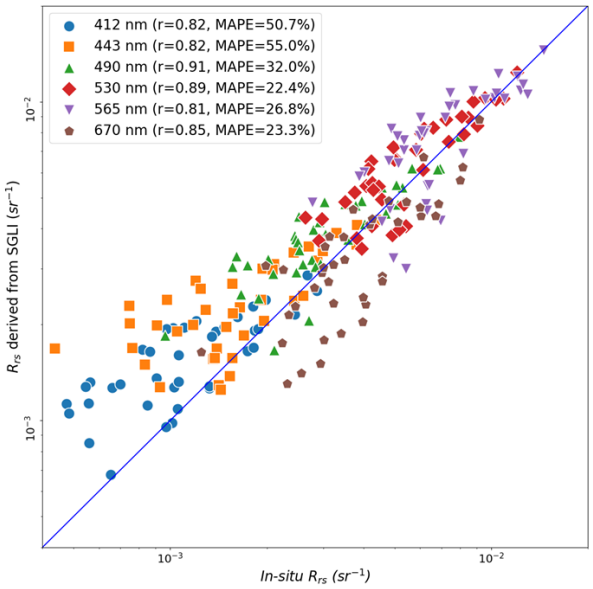


Figure 6. Comparison of remote sensing reflectance (R_{rs}) between the GCOM-C/SGLI satellite-derived and in situ measurements at the observed wavelengths of the SGLI across 10 sampling stations in Lake Kasumigaura.

3.3. Correlation Between the Algorithm-Derived IOPs and the Measured Water Quality Parameters

The correlation of IOPs and the monitoring of biogeochemical properties have the potential to further our understanding of aquatic environments [107]. The correlation between these IOPs and biogeochemical parameters was analyzed using Pearson correlation heatmaps (Figure 7). To elucidate the specific characteristics of IOPs and their relationships with biogeochemical properties, it is essential to differentiate between the various IOP components. The study found distinct patterns in the correlation of IOPs, derived from the QAA, with measured water quality parameters (i.e., Chl-a, POC, PON, DON, and SS) across various wavelengths of IOPs. These findings underscore the effectiveness of $a_p(\lambda)$, $a_{ph}(\lambda)$, and $a_{NAP}(\lambda)$ derived using the QAA and $a_{CDOM}(\lambda)$ derived using the GSM algorithm in identifying correlations between IOPs and in situ biogeochemical parameters.

Parameter $a_p(\lambda)$, derived using the QAA, showed associations with various biogeochemical parameters, with significant correlations across different wavelengths. The particle absorption correlation coefficient at 443 nm had a strong correlation with Chl-a, with a coefficient of 0.7, and positive correlations across wavelengths, ranging from 0.35 to 0.70. Phytoplankton cells contain pigments, including Chl-a, that absorb light at specific wavelengths, contributing to the overall particle absorption [108]. The particle absorption at 565 nm correlated well with POC, showing a correlation of 0.63, with consistent correlations (0.25 to 0.63) across wavelengths. Similarly, the correlation with PON at 565 nm was 0.66, with a positive correlation (0.29 to 0.66) across wavelengths. POC and PON are components of organic matter associated with particles, such as phytoplankton, detritus, and other suspended organic materials [47,109]. Light absorption by these particles is thus influenced by the concentration of organic matter, particularly pigments and light-absorbing organic matter [110]. The correlation with DON was weaker, peaking at 0.32 and generally being weak across wavelengths. For organic SS, a correlation of 0.66 was observed at 565 nm, with high correlations (0.27 to 0.66) across wavelengths. Organic SS are a major contributor to particle absorption as they include a variety of organic particles, such as detritus, microorganisms, and aggregated organic matter [111]. In contrast, inorganic SS exhibited negative-to-weak correlations with $a_p(\lambda)$.

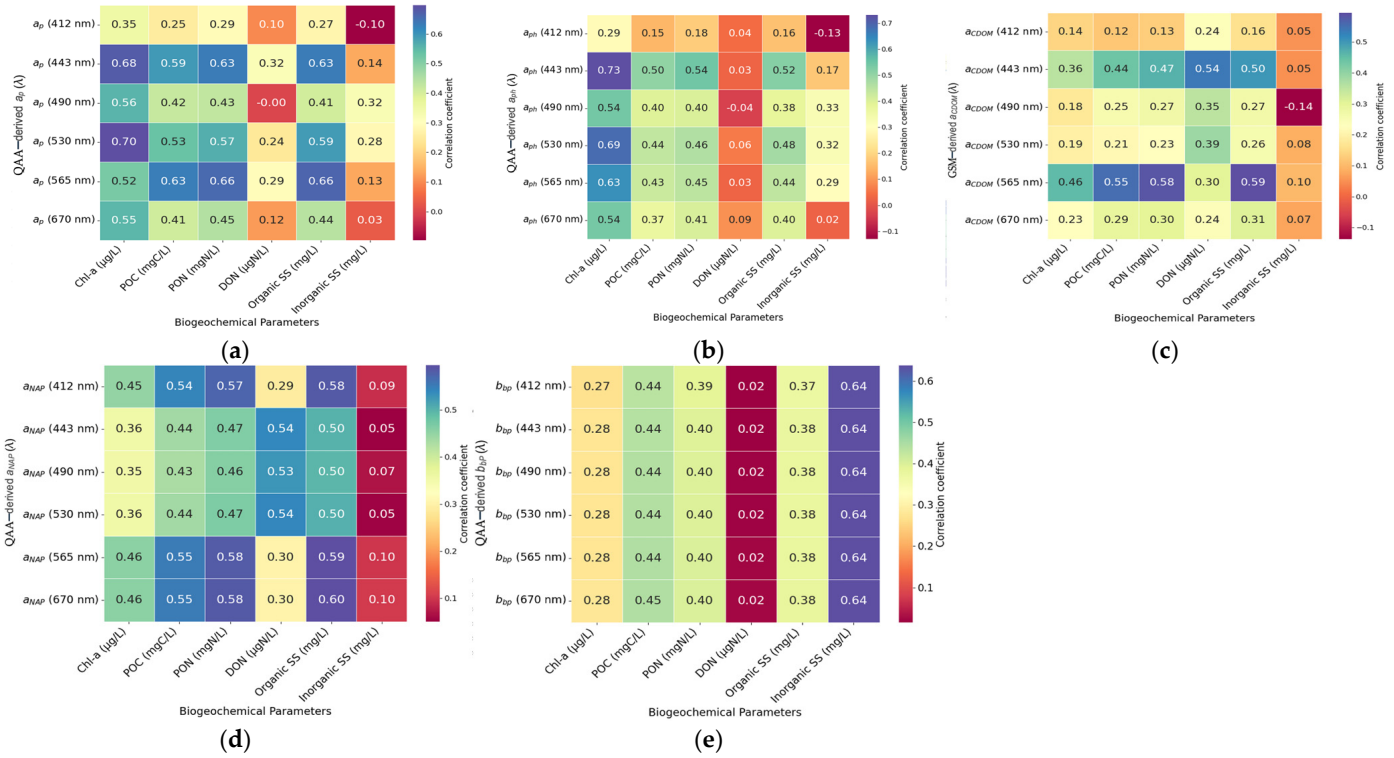


Figure 7. Correlation heatmaps showing the relationships between the IOPs derived by using the SGLI R_{rs} and biogeochemical parameters. The heatmap specifically analyzes (**a**) a_p, (**b**) a_{ph}, (**c**) a_{CDOM}, (**d**) a_{NAP}, and (**e**) b_{bp} across six wavelengths (412, 443, 490, 530, 565, and 670 nm). These optical properties are correlated with biogeochemical variables, including Chl-a, POC, PON, DON, organic and inorganic SS.

The correlation analysis of the QAA-derived a_{ph} at selected wavelengths with different water quality parameters revealed a range of relationships, underscoring the complex interactions within aquatic ecosystems. Chl-a exhibited a strong positive correlation with a_{ph}, particularly at 443 nm (r = 0.73), because it is a primary pigment in phytoplankton and directly responsible for light absorption in the blue spectrum; phytoplankton absorption is thus closely linked to Chl-a concentration [108]. However, a_{ph} at 412 nm showed weak correlations with most water quality parameters. Positive correlations were observed between a_{ph} and POC (r = 0.15 to 0.5) and PON (r = 0.18 to 0.54). The correlation of particulate organic materials is associated with phytoplankton, which contributes to the overall absorption properties of the water [47]. DON was generally low and had a negative correlation with a_{ph}. Organic SS had a moderate correlation with a_{ph} (r = 0.15 to 0.52) because they often originate from decomposing phytoplankton and other organic matter, contributing to light absorption. In contrast, inorganic SS generally show low correlations with phytoplankton absorption. This is likely due to inorganic SS primarily scattering light rather than absorbing light.

Parameter $a_{CDOM}(\lambda)$ derived from using the GSM algorithm was examined in relation to various biogeochemical parameters, revealing correlations across wavelengths. The correlation of a_{CDOM} with dissolved nutrients allows for the determination of DON concentrations [112]. Absorption by colored DON is influenced by the mass of dissolved matter and organic SS in water [113,114]. The a_{CDOM} at 443 nm had a moderate correlation with Chl-a, with a coefficient of 0.46, and showed positive correlations across wavelengths. As phytoplankton (which contains Chl-a) grows and decomposes, it releases organic materials, including a_{CDOM} [108]. Parameter a_{CDOM} at 565 nm showed a moderate correlation with POC and PON, with a correlation of 0.53 and 0.51, demonstrating

positive correlations across wavelengths. The correlation with DON was high, reaching 0.60, with positive correlations (0.49 to 0.60) across wavelengths. This suggests that a_{CDOM} is a useful indicator for assessing DON concentrations [115,116]. Since both DON and a_{CDOM} are derived from the breakdown of organic matter, their concentrations are correlated [117]. The correlation with organic SS was also high (0.59 at 565 nm); it showed a positive correlation across all wavelengths. The strength of this correlation depends on environmental conditions, sources of organic matter, and the characteristics of the given aquatic environment [34]. Inorganic SS, however, displayed negative-to-weak correlations with $a_{CDOM}(\lambda)$.

The relationship between the QAA-derived $a_{NAP}(\lambda)$ and various biogeochemical parameters was investigated. Several key correlations were found across different wavelengths. The NAP absorption coefficient at 565 nm exhibited a moderate correlation with Chl-a, with a coefficient of 0.46, and had positive correlations across wavelengths, ranging from 0.35 to 0.46. Higher Chl-a leads to an increase in the production of organic detritus, which contributes to the pool of non-algal particles as phytoplankton cells die and break down. The absorption at 565 and 670 nm showed strong correlations with POC, with a correlation of 0.55, and maintained high correlations (0.43 to 0.55) across wavelengths. Similarly, the correlation with PON at 565 and 670 nm was 0.58, showing moderate-to-high correlations (0.46 to 0.58) across wavelengths. The correlation of a_{NAP} with POC and PON depends on the composition of the particulate matter in the water and the specific environmental conditions [109]. A positive correlation was observed between a_{NAP} and particulate organic matter. The correlation with DOM was 0.54 at 443 and 530 nm, with positive correlations across wavelengths, ranging from 0.24 to 0.54. The correlation with organic SS peaked at 0.6 at 670 nm, showing the best correlations (0.5 and 0.6) across wavelengths. In contrast, inorganic SS exhibited negative-to-weak correlations with $a_{NAP}(\lambda)$.

The correlation analysis of the QAA-derived b_{bp} at different wavelengths with various water quality parameters revealed significant relationships with the optical properties of the water body. The correlation between b_{bp} and Chl-a was generally low, with values around 0.28 across different wavelengths. This is likely because Chl-a, primarily associated with light absorption, contributes less to the particulate matter that influences backscattering. In contrast, b_{bp} showed moderate-to-substantial positive correlations with POC and PON, ranging from 0.40 to 0.45. This indicates that particulate organic materials likely contribute to the backscattering properties, enhancing the light scattering by particles in the water [118,119]. On the other hand, b_{bp} exhibited a weak positive correlation with organic SS (around 0.38), reflecting the role of organic SS in light scattering. Notably, b_{bp} had strong correlations with inorganic SS, with a consistent value of 0.64 across all wavelengths, highlighting the significant impact of inorganic particles on light backscattering.

4. Discussion

4.1. Performance Evaluation of IOP Algorithms and Validation of R_{rs}

The performance of the IOP retrieval algorithms across IOPs and wavelengths highlights significant differences in accuracy and reliability. The QAA consistently outperformed other algorithms, demonstrating the lowest error metrics and the highest correlation coefficients for most parameters. For $a_p(\lambda)$ and $a_{ph}(\lambda)$, the QAA achieved the highest accuracy with low MAPE and RMSE and high correlation coefficients. This performance is corroborated by previous studies [10,27,29] that emphasized the QAA's ability to provide precise absorption estimates. The QAA outperforms other IOP retrieval algorithms in eutrophic lakes due to its semi-analytical, spectrally adaptive approach, which effectively decouples absorption and backscattering even in eutrophic waters [10]. In contrast, the GSM algorithm, while achieving a reasonable correlation for $a_p(\lambda)$, exhibited

higher MAPE and RMSE, indicating greater variability in its estimations [105]. The PML and LMI algorithms showed weaker performance, with lower *r* values and higher error metrics. The GIOP algorithm followed with reasonable error metrics, supporting its competitive accuracy as noted by Jorge et al. [27] and Werdell et al. [26].

The GSM algorithm exhibited a slightly better performance for estimating both $a_{NAP}(\lambda)$ and $a_{CDOM}(\lambda)$, highlighting its robustness and potential for deriving $a_{dg}(\lambda)$ [11]. This makes it a valuable tool for applications in aquatic optics, particularly in environments where precise separation of absorption components is critical. However, the QAA performed slightly better, with a higher correlation coefficient. For $a_{CDOM}(\lambda)$, the GSM algorithm achieved the highest correlation, with lower errors, aligning with the results obtained by Betancur-Turizo et al. [11] and Lewis and Arrigo [106]. GSM's robustness in retrieving CDOM-dominated absorption is attributed to its semi-empirical parameterization of a_{CDOM} spectral slopes [28]. The GIOP algorithm had moderate accuracy, while the PML algorithm showed the weakest performance, with the lowest correlation and the highest MAPE and RMSE values.

The GIOP algorithm demonstrated a competitive performance for $a_{ph}(\lambda)$ and $a_{NAP}(\lambda)$, although it was not as consistently accurate as the QAA or GSM algorithms [27,29]. In eutrophic environments, both the QAA and GIOP algorithms show potential for accurately deriving absorption coefficients. Specifically, GIOP outperformed the PML and LMI algorithms for estimating $a_{ph}(\lambda)$, achieving better correlation coefficients. Additionally, GIOP demonstrated lower error metrics, suggesting its suitability for use with further fine-tuning [10]. These results highlight the robustness of GIOP in eutrophic conditions, making it a promising tool for deriving absorption properties in complex aquatic environments. For $a_{NAP}(\lambda)$, GIOP's performance was similar to that of LMI and PML, with slightly higher error metrics. These findings suggest that while GIOP is not the most robust algorithm, additional parameterizations are needed for highly eutrophic environments [27], but its competitive performance in specific scenarios positions it as a viable alternative, particularly when optimized for specific optical conditions [10,120].

The performance of IOP algorithms depends on the optical water class and underlying equations used in their development, which can significantly influence their accuracy and effectiveness [11,27]. The PML and LMI algorithms exhibited a weaker performance, as evidenced by their higher error metrics and lower correlation coefficients across most IOPs. For $a_{CDOM}(\lambda)$, the PML algorithm showed the highest MAPE and RMSE among all algorithms, with a significantly lower correlation coefficient, indicating its limited accuracy in retrieving a_{CDOM}. Similarly, for $a_{ph}(\lambda)$, PML's performance was poor, reflecting its inability to accurately handle phytoplankton absorption. The LMI algorithm demonstrated a similarly inconsistent performance, with moderate error metrics for $a_{CDOM}(\lambda)$ and $a_{ph}(\lambda)$ but a lower correlation coefficient [120]. These weaknesses underline the limitations of PML and LMI in accurately retrieving IOPs compared to the more robust QAA and GSM algorithms.

For shorter wavelengths, the error metrics were higher for algorithms such as the GSM algorithm, indicating potential issues with signal attenuation or noise [29]. Despite the variability observed for the GSM algorithm at lower wavelengths, there were notable similarities between the results of the GIOP and GSM algorithms, both of which utilize the Levenberg–Marquardt algorithm for solving unconstrained nonlinear least-squares problems [11]. The QAA and the GSM algorithm have the best accuracy, with consistent low error metrics and high correlation coefficients across various conditions [27]. The GIOP algorithm has potential but requires further tuning and optimization to improve its accuracy and reduce its variability [120]. Given the limitations of shorter wavelengths in complex hydrodynamic conditions within aquatic environments, longer wavelengths

are increasingly being recognized for their enhanced utility in characterizing the optical properties of water [10].

The accuracy assessment of R_{rs} shows that there is a generally strong correlation between GCOM-C/SGLI satellite imagery and in situ data, particularly at higher wavelengths. Improvements in satellite data processing, atmospheric correction algorithms, and calibration/validation procedures could enhance the accuracy of satellite-estimated R_{rs} across all wavelengths [19,26,29,121]. Despite the challenges posed by the highly eutrophic conditions of Lake Kasumigaura, remote sensing reflectance-based water quality indicators have been successfully applied to estimate key parameters such as Chl-a and SS, demonstrating their utility in reducing uncertainty in optically complex waters [16,122–124]. Moreover, integrating satellite data with in situ measurements and advanced modeling techniques may improve the reliability and application of satellite-based water quality assessments [125,126]. Atmospheric correction improves retrieval of IOPs by minimizing aerosol overestimation in high-turbidity regimes, and these improvements preserve the spectral integrity of subsurface optical properties, which is critical for deriving *aph*, a_{NAP}, a_{CDOM}, and b_{bp} in chlorophyll-rich waters [26]. Aerosol models and sun glint parallax correction further reduce uncertainties in coastal and inland waters, where complex aerosol mixtures and surface glare often obscure the water-leaving signal needed for accurate IOP inversion [124,127].

The correlation analysis of water optical properties with various water quality parameters revealed that relationships varied based on the characteristics of the water components and their effects on light absorption and scattering. The QAA-derived a_p at 443 and 530 nm exhibited a strong correlation with Chl-a and had a moderate correlation with POC, PON, and organic suspended solids. This moderate-to-strong relationship reflects the combined contributions of phytoplankton pigments, particulate organic matter, detritus, and non-algal particles to the total particle absorption [47]. The QAA-derived a_{ph} at 443 and 530 nm showed high correlations with Chl-a (r = 0.69 and r = 0.73), Supporting studies indicating QAA-derived IOPs (especially a_{ph}) as effective Chl-a proxies [41,46,128,129]. GSM-derived a_{CDOM} at 443 nm exhibited positive correlations (r = 0.54) with DON, indicating that a_{CDOM} has the potential to serve as a proxy for detecting dissolved organic matter. [130]. The QAA-derived a_{NAP} at 443, 530, and 670 nm exhibited positive correlations with POC, PON, and organic suspended solids, underscoring the significant role of organic components in water optical properties by contributing to light absorption [46,47,131]. Conversely, inorganic SS showed strong positive correlations with b_{bp} (r = 0.64), reflecting the substantial influence of inorganic particles on light scattering, which is crucial for understanding water clarity and particle concentration [132]. The high interrelationship among backscattering coefficients across different wavelengths, particularly with inorganic SS, emphasizes how these particles dominate light scattering in water [133]. These findings highlight the importance of specific wavelengths in monitoring water quality, with different optical properties providing valuable insights into the presence and concentration of both organic and inorganic matter in aquatic environments.

This study evaluated the performance of commonly applied IOP algorithms for water quality monitoring in highly eutrophic lakes, incorporating validation with in situ measurements and satellite data. A key limitation arises from the inherent optical complexity of such environments, which can significantly impair the accuracy of IOP retrievals [134]. High variability in water constituents, including dissolved organic matter, suspended sediments, and phytoplankton, introduces challenges in isolating distinct optical signatures [21,135]. Furthermore, atmospheric interference, particularly due to light scattering and absorption, introduces additional uncertainties in remote sensing data, affecting water quality assessments [20,59,124]. Given the high sensitivity of IOP algorithms

to minor perturbations [27], these environmental and atmospheric factors may reduce the reliability of derived biogeochemical parameters.

4.2. Comparison of Phytoplankton Absorption and Chlorophyll a

Understanding Chl-a and phytoplankton absorption is crucial for monitoring aquatic environments and evaluating the impact of environmental changes on primary production and nutrient dynamics [136,137]. Standard GCOM-C/SGLI algorithms have been developed through empirical approaches to enable cross-sensor compatibility for chlorophyll a (Chl-a) estimation [138].

The correlation between Chl-a and a_{ph} (443 nm) indicated good accuracy, with a linear correlation of r = 0.73 (Figure 7b) and a polynomial correlation of r = 0.84 (Figure 8a,b). A polynomial function was subsequently developed to derive Chl-a using a_{ph} (443 nm), reflecting this enhanced relationship.

$$\text{Chl} - \text{a} \;=\; -236.43 \times a_{ph}(443\ \text{nm})^2 + 336.76 \times a_{ph}\ (443\ \text{nm}) - 12.89 \qquad (10)$$

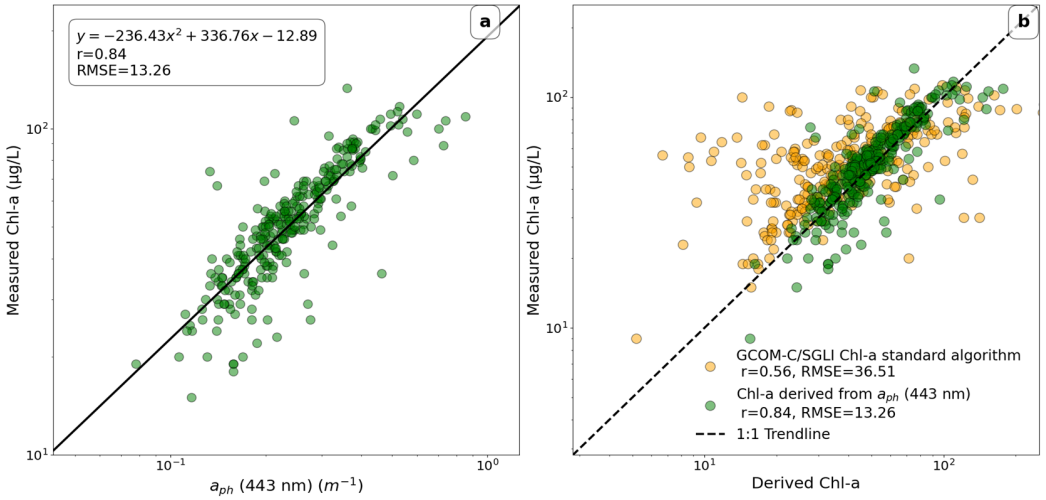


Figure 8. Scatter graph of (**a**) the QAA-derived a_{ph} at 443 nm with measured Chl-a (µg/L) and (**b**) comparison of the derived Chl-a (µg/L) with the measured Chl-a (µg/L).

From the comparison of the correlation between the Chl-a concentration and a_{ph} at different wavelengths, alongside the derived Chl-a values, the correlation coefficient for Chl-a measured against a_{ph} at 443 nm was 0.84, and the RMSE value was 13.26 µg/L, indicating a good relationship between the Chl-a concentration and phytoplankton absorption at this wavelength due to the dominant absorption characteristics of photosynthetic pigments in the blue spectral region [139]. This relationship forms the basis for many bio-optical algorithms that estimate Chl-a from remote sensing reflectance, particularly in open ocean waters where phytoplankton pigments dominate the optical signature [140]. This result is due to the varying absorption efficiency of phytoplankton pigments, which absorb more strongly in the blue region and less in other regions, thereby affecting the relationship with Chl-a. In contrast, the Chl-a values that Murakami [138] derived had a correlation coefficient of 0.56 and RMSE values of 36.51 µg/L, and the Chl-a estimated based on a_{ph} (443 nm) had a correlation coefficient of 0.84 and the RMSE value of 13.26 µg/L, respectively. The Chl-a values estimated based on a_{ph} (443 nm) had a better correlation, which indicates that absorption by phytoplankton is a good indicator of Chl-a in Lake Kasumigaura. However, the strength of the correlation and potential estimation errors must be considered. This method outperformed remote sensing reflectance-based Chl-a estimations, which achieved a validation r of 0.65 [16]. Spectral decomposition analysis

(SDA) has exhibited comparative performance at Lake Kasumigaura [64,65]. To assess the Chl-a concentration, the right combination of a_{ph} can be used based on phytoplankton biomass in water quality assessments [141,142]. This indicates that IOP-based algorithms can be applied for water quality estimation [18].

4.3. Comparison of the Correlation Between Backscattering of Particles and Suspended Solids

High particle concentrations significantly affect light backscattering in water by altering backscattering coefficients and spectral properties. Studies have shown that the measured backscatter intensity can be used to estimate SS based on particle size distributions and concentrations [57,58]. Additionally, particle backscattering is crucial for estimating SS in highly turbid coastal waters, underscoring the importance of understanding the interactions between backscattering coefficients and suspended particles [55,56]. The increase in turbidity at Lake Kasumigaura is likely attributable to sediment suspension and higher inorganic SS [122].

The analysis of water optical properties, particularly the relationship between SS and backscattering at 443 nm, reveals important distinctions between organic and inorganic suspended particles. The correlation between organic SS and water optical properties (Figure 9a), specifically backscattering at 443 nm, was weak (r = 0.38 and RMSE = 0.24 mg/L) because other optically active substances in organic SS, such as phytoplankton, non-algal particles, and DOM, have absorption properties. The complex nature of particulate organic matter, which predominantly absorbs light rather than scattering it, limits the contribution of organic matter to backscattering signals. For inorganic SS, the correlation with b_{bp} (443 nm) (Figure 9b) was high (r = 0.64 and RMSE = 25.05 mg/L). The backscattering of particles at 443 nm provides good insight into inorganic suspended particles [47]. The correlation of suspended solids and backscattering indicates distinct optical properties, where organic and inorganic components interact differently with light. The backscattering at 443 nm is a good indicator for assessing inorganic suspended particles, offering valuable insights into water quality and particle composition [46,131]. The b_{bp}-based estimation of inorganic SS has significant potential to be accurate, especially if refined methodologies are employed or additional parameters are considered.

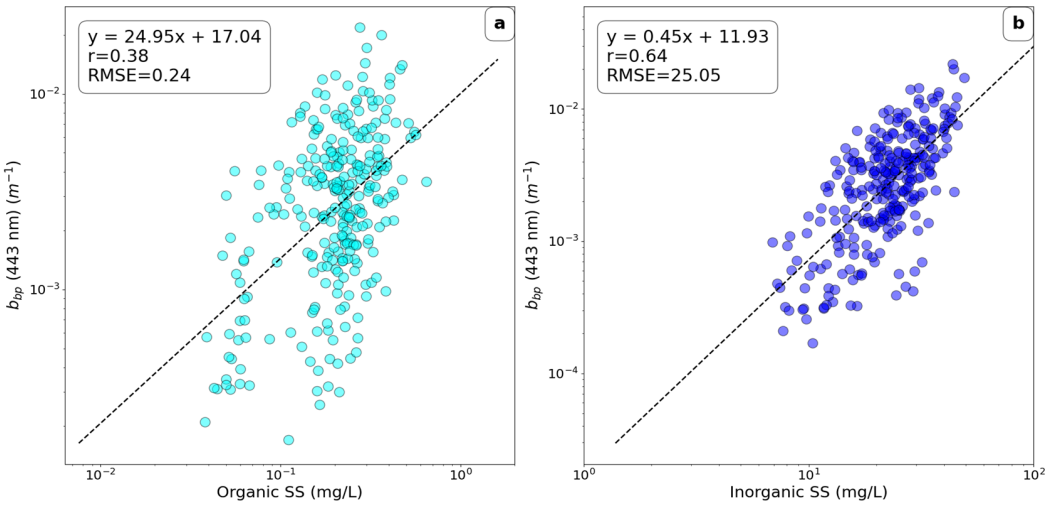


Figure 9. Correlation of b_{bp} (443 nm) with (**a**) organic SS (mg/L) and (**b**) inorganic SS (mg/L).

5. Conclusions

In this study, the performance of the QAA, PML, LMI, GIOP, and GSM IOP algorithms at Lake Kasumigaura, Japan, were investigated. A comparison of the IOP algorithms across different wavelengths and IOPs was conducted based on the key metrics, including the

correlation coefficient. Notably, the QAA demonstrated a consistently superior performance for $a_p(\lambda)$, $a_{ph}(\lambda)$, and $a_{NAP}(\lambda)$, as indicated by its low MAPE and RMSE values (0.23 m^{-1} and 0.08 m^{-1}) and a high correlation coefficient (0.85 to 0.98). The GSM algorithm had the highest correlation for $a_{CDOM}(\lambda)$, indicating its reliability across a spectrum of conditions at Lake Kasumigaura. The PML and LMI algorithms showed relatively high error rates, particularly at shorter wavelengths, indicating potential discrepancies in their estimations and limitations in their application at these specific spectral bands. Based on the comparative analysis of the IOP algorithms, the QAA and the GSM algorithms were chosen for the analysis of the implications of IOPs on water quality due to their higher correlation coefficients, lower MAPE and RMSE, and strong consistency.

The accuracy assessment of the level 2 GCOM-C/SGLI satellite-derived R_{rs} compared with the in situ measured R_{rs} showed a strong correlation at mid-to-longer wavelengths and a moderate correlation at shorter wavelengths. Reliability of satellite-derived R_{rs} is crucial for the effective application of IOP algorithms. Studies have highlighted the critical need for improved atmospheric correction techniques, particularly at lower wavelengths, to enhance the accuracy and reliability of remote sensing data across various applications. The correlation analysis of the QAA-derived IOPs with the measured water quality parameters showed a significant correlation in that a_{ph} at 443 nm correlated well with the Chl-a concentration (r = 0.84, RMSE = 13.26 μg/L) and that b_{bp} at 443 nm correlated well with inorganic SS (r = 0.64, RMSE = 25.05 mg/L). These findings highlight that the different levels of correlation of IOPs serve as indicators of Chl-a, POC, PON, DON, and both organic and inorganic SS at Lake Kasumigaura. Improving the predictive accuracy of water quality by employing advanced methods and incorporating additional environmental factors can enhance long-term water quality monitoring in eutrophic lakes, particularly by using IOPs alongside satellite remote sensing data.

Author Contributions: Conceptualization, H.H. and M.C.; methodology, H.H. and M.C.; analysis, H.H. and M.C.; visualization, H.H. and M.C.; supervision, H.H.; writing—review and editing, M.C., H.H., S.I.S., E.S., T.S. and M.M. All authors have read and agreed to the published version of the manuscript.

Funding: The Japan Aerospace Exploration Agency (JAXA) funded this research under the Research Announcement on Earth Observations (EO-RA3). The Japan Society for the Promotion of Science (JSPS) KAKENHI also provided support through the Grant-in-Aid for Early-Career Scientists, with grant numbers 20K14836 and 22H05716.

Data Availability Statement: The original contributions presented in the study are included in the article, further inquiries can be directed to the corresponding author.

Acknowledgments: The first author would like to express heartfelt gratitude to the Japanese government for awarding the MEXT (Ministry of Education, Culture, Sports, Science, and Technology) scholarship, which made this research possible. The measured water quality data are those of the Lake Kasumigaura Long-term Environmental Monitoring Program of the National Institute for Environmental Studies, Japan. The authors are also deeply grateful to the Japan Aerospace Exploration Agency (JAXA) for supplying level 2 SGLI data through the Global Change Observation Mission for Climate (GCOM-C).

Conflicts of Interest: The authors declare that there are no conflicts of interest regarding the publication of this article. The research was conducted independently and without any external influence that could have affected the objectivity or integrity of the results and conclusions presented.

References

1. Fang, C.; Song, C.; Wang, X.; Wang, Q.; Tao, H.; Wang, X.; Ma, Y.; Song, K. A novel total phosphorus concentration retrieval method based on two-line classification in lakes and reservoirs across China. *Sci. Total Environ.* **2024**, *906*, 167522. [CrossRef] [PubMed]
2. Seegers, B.N.; Werdell, P.J.; Vandermeulen, R.A.; Salls, W.; Stumpf, R.P.; Schaeffer, B.A.; Owens, T.J.; Bailey, S.W.; Scott, J.P.; Loftin, K.A. Satellites for long-term monitoring of inland U.S. lakes: The MERIS time series and application for chlorophyll-a. *Remote Sens. Environ.* **2021**, *266*, 112685. [CrossRef] [PubMed]
3. Cao, Z.; Shen, M.; Kutser, T.; Liu, M.; Qi, T.; Ma, J.; Ma, R.; Duan, H. What water color parameters could be mapped using MODIS land reflectance products: A global evaluation over coastal and inland waters. *Earth-Science Rev.* **2022**, *232*, 104154. [CrossRef]
4. Wang, S.; Li, J.; Zhang, B.; Lee, Z.; Spyrakos, E.; Feng, L.; Liu, C.; Zhao, H.; Wu, Y.; Zhu, L.; et al. Changes of water clarity in large lakes and reservoirs across China observed from long-term MODIS. *Remote Sens. Environ.* **2020**, *247*, 111949. [CrossRef]
5. Kapalanga, T.S.; Hoko, Z.; Gumindoga, W.; Chikwiramakomo, L. Remote-sensing-based algorithms for water quality monitoring in olushandja dam, north-central namibia. *Water Supply* **2021**, *21*, 1878–1894. [CrossRef]
6. Krishna, S.; Ulloa, H.N.; Barbe, E.; Wüest, A. Disentangling the effects of climate change and reoligotrophication on primary production in a large lake. *Aquat. Sci.* **2023**, *85*, 16. [CrossRef]
7. Ayala, A.I.; Mesman, J.P.; Jones, I.D.; de Eyto, E.; Jennings, E.; Goyette, S.; Pierson, D.C. Climate Change Impacts on Surface Heat Fluxes in a Deep Monomictic Lake. *J. Geophys. Res. Atmos.* **2023**, *128*, e2022JD038355. [CrossRef]
8. Fathi, E.; Zamani-Ahmadmahmoodi, R.; Zare-Bidaki, R. Water quality evaluation using water quality index and multivariate methods, Beheshtabad River, Iran. *Appl. Water Sci.* **2018**, *8*, 210. [CrossRef]
9. Holzbauer-Schweitzer, B.K.; Nairn, R.W. In-situ manipulations of aquatic optical depth and its effect on small unoccupied aerial systems–derived spectral reflectance. *Drone Syst. Appl.* **2022**, *10*, 427–443. [CrossRef]
10. Najah, A.; Al-Shehhi, M.R. Performance of the Ocean Color Algorithms: QAA, GSM, and GIOP in Inland and Coastal Waters. *Remote Sens. Earth Syst. Sci.* **2021**, *4*, 235–248. [CrossRef]
11. Betancur-Turizo, S.P.; González-Silvera, A.; Santamaría-del-ángel, E.; Tan, J.; Frouin, R. Evaluation of semi-analytical algorithms to retrieve particulate and dissolved absorption coefficients in Gulf of California optically complex waters. *Remote Sens.* **2018**, *10*, 1443. [CrossRef]
12. Glukhovets, D. An Overview of the Special Issue on Seawater Bio-Optical Characteristics from Satellite Ocean Color Data. *Remote Sens.* **2023**, *15*, 1094. [CrossRef]
13. van Oostende, M.; Hieronymi, M.; Krasemann, H.; Baschek, B. Global ocean colour trends in biogeochemical provinces. *Front. Mar. Sci.* **2023**, *10*, 1052166. [CrossRef]
14. El Kassar, J.; Juhls, B.; Hieronymi, M.; Preusker, R.; Morgenstern, A.; Fischer, J.; Overduin, P.P. Optical remote sensing (Sentinel-3 OLCI) used to monitor dissolved organic carbon in the Lena River, Russia. *Front. Mar. Sci.* **2023**, *10*, 1082109. [CrossRef]
15. Higa, H.; Sugahara, S.; Salem, S.I.; Nakamura, Y.; Suzuki, T. An estimation method for blue tide distribution in Tokyo Bay based on sulfur concentrations using Geostationary Ocean Color Imager (GOCI). *Estuar. Coast. Shelf Sci.* **2020**, *235*, 106615. [CrossRef]
16. Salem, S.I.; Strand, M.H.; Higa, H.; Kim, H.; Kazuhiro, K.; Oki, K.; Oki, T. Evaluation of meris chlorophyll-a retrieval processors in a complex turbid lake kasumigaura over a 10-year mission. *Remote Sens.* **2017**, *9*, 1022. [CrossRef]
17. Dalin, J. Estimation of Water Transparency from Remote Sensing Data Based on A New Underwater Visibility Theory. 2020. Available online: https://tsukuba.repo.nii.ac.jp/record/55096/files/DA09505.pdf (accessed on 5 September 2024).
18. Chen, M.; Xiao, F.; Wang, Z.; Feng, Q.; Ban, X.; Zhou, Y.; Hu, Z. An Improved QAA-Based Method for Monitoring Water Clarity of Honghu Lake Using Landsat TM, ETM+ and OLI Data. *Remote Sens.* **2022**, *14*, 3798. [CrossRef]
19. Higa, H.; Muto, M.; Salem, S.I.; Kobayashi, H.; Ishizaka, J.; Ogata, K.; Toratani, M.; Takahashi, K.; Maupin, F.; Victori, S. Optical Characterization of Coastal Waters with Atmospheric Correction Errors: Insights from SGLI and AERONET-OC. *Remote Sens.* **2024**, *16*, 3626. [CrossRef]
20. Ahmed, M.; Mumtaz, R.; Anwar, Z.; Shaukat, A.; Arif, O.; Shafait, F. A Multi–Step Approach for Optically Active and Inactive Water Quality Parameter Estimation Using Deep Learning and Remote Sensing. *Water* **2022**, *14*, 2112. [CrossRef]
21. Li, L.; Li, L.; Song, K.; Li, Y.; Tedesco, L.P.; Shi, K.; Li, Z. An inversion model for deriving inherent optical properties of inland waters: Establishment, validation and application. *Remote Sens. Environ.* **2013**, *135*, 150–166. [CrossRef]
22. Kerrisk, G.; Drayson, N.; Ford, P.; Botha, H.; Anstee, J. Performance assessment of serial dilutions for the determination of backscattering properties in highly turbid waters. *Limnol. Oceanogr. Methods* **2023**, *21*, 243–258. [CrossRef]
23. Zaneveld, R.; Barnard, A.; Lee, Z. Remote Sensing of Inherent Optical Properties: Fundamentals, Tests of Algorithms, and Applications. 2006. Available online: https://ioccg.org/reports/report5.pdf (accessed on 11 September 2024).
24. Lee, Z.; Lubac, B.; Werdell, J.; Arnone, R. An Update of the Quasi-Analytical Algorithm (QAA_v5). *Int. Ocean. Color Group Softw. Rep.* **2009**, *1*, 1–9.
25. Lee, Z.; Carder, K.L.; Arnone, R.A. Deriving inherent optical properties from water color: A multiband quasi-analytical algorithm for optically deep waters. *Appl. Opt.* **2002**, *41*, 5755. [CrossRef]

26. Werdell, P.J.; Franz, B.A.; Bailey, S.W.; Feldman, G.C.; Boss, E.; Brando, V.E.; Dowell, M.; Hirata, T.; Lavender, S.J.; Lee, Z.; et al. Generalized Ocean color inversion model for retrieving marine inherent optical properties. *Appl. Opt.* **2013**, *52*, 2019–2037. [CrossRef] [PubMed]
27. Jorge, D.S.F.; Loisel, H.; Jamet, C.; Dessailly, D.; Demaria, J.; Bricaud, A.; Maritorena, S.; Zhang, X.; Antoine, D.; Kutser, T.; et al. A three-step semi analytical algorithm (3SAA) for estimating inherent optical properties over oceanic, coastal, and inland waters from remote sensing reflectance. *Remote Sens. Environ.* **2021**, *263*, 112537. [CrossRef]
28. Maritorena, S.; Siegel, D.A. Consistent merging of satellite ocean color data sets using a bio-optical model. *Remote Sens. Environ.* **2005**, *94*, 429–440. [CrossRef]
29. Deng, L.; Zhou, W.; Cao, W.; Wang, G.; Zheng, W.; Xu, Z.; Li, C.; Yang, Y.; Xu, W.; Zeng, K.; et al. Evaluating semi-analytical algorithms for estimating inherent optical properties in the South China Sea. *Opt. Express* **2020**, *28*, 13155. [CrossRef]
30. Smyth, T.J.; Moore, G.F.; Hirata, T.; Aiken, J. Semianalytical model for the derivation of ocean color inherent optical properties: Description, implementation, and performance assessment. *Appl. Opt.* **2006**, *45*, 8116–8131. [CrossRef]
31. Hoge, F.E.; Lyon, P.E. Satellite retrieval of inherent optical properties by linear matrix inversion of oceanic radiance models: An analysis of model and radiance measurement errors. *J. Geophys. Res. Ocean.* **1996**, *101*, 16631–16648. [CrossRef]
32. Hoge, F.E.; Lyon, P.E. New tools for the study of oceanic eddies: Satellite derived inherent optical properties. *Remote Sens. Environ.* **2005**, *95*, 444–452. [CrossRef]
33. Chen, J.; Quan, W.; Duan, H.; Xing, Q.; Xu, N. An Improved Inherent Optical Properties Data Processing System for Residual Error Correction in Turbid Natural Waters. *IEEE J. Sel. Top. Appl. Earth Obs. Remote Sens.* **2021**, *14*, 6596–6607. [CrossRef]
34. Dall'olmo, G.; Gitelson, A.A. Absorption Properties of Dissolved and Particulate Matter in Turbid Productive Inland Lakes. In Proceedings of the Ocean Optics XVII, Montreal, QC, Canada, 9–13 October 2006. Available online: https://scispace.com/pdf/absorption-properties-of-dissolved-and-particulate-matt-er-38olblnet7.pdf (accessed on 6 October 2024).
35. Xue, K.; Boss, E.; Ma, R.; Shen, M. Algorithm to derive inherent optical properties from remote sensing reflectance in turbid and eutrophic lakes. *Appl. Opt.* **2019**, *58*, 8549. [CrossRef]
36. Xue, K.; Ma, R.; Shen, M.; Wu, J.; Hu, M.; Guo, Y.; Cao, Z.; Xiong, J. Horizontal and vertical migration of cyanobacterial blooms in two eutrophic lakes observed from the GOCI satellite. *Water Res.* **2023**, *240*, 120099. [CrossRef]
37. Feng, C.; Zhu, Y.; Shen, A.; Li, C.; Song, Q.; Tao, B.; Zeng, J. Assessment of GCOM-C Satellite Imagery in Bloom Detection: A Case Study in the East China Sea. *Remote Sens.* **2023**, *15*, 691. [CrossRef]
38. Shi, W.; Wang, M. A blended inherent optical property algorithm for global satellite ocean color observations. *Limnol. Oceanogr. Methods* **2019**, *17*, 377–394. [CrossRef]
39. Bracher, A.; Bouman, H.A.; Brewin, R.J.W.; Bricaud, A.; Brotas, V.; Ciotti, A.M.; Clementson, L.; Devred, E.; Di Cicco, A.; Dutkiewicz, S.; et al. Obtaining phytoplankton diversity from ocean color: A scientific roadmap for future development. *Front. Mar. Sci.* **2017**, *4*, 55. [CrossRef]
40. Pegau, S.; Zunefeld, J.R.; Mitchell, B.G.; Muellel, J.L.; Kahru, M.; Wieland, J.; Stramska, M. Ocean Optics Protocols for Satellite Ocean Color Sensor Validation, Rev. 4, Vol. IV: Inherent Optical Properties: Instruments, Characterisations, Field Measurements and Data Analysis Protocols. 2003. Available online: https://ntrs.nasa.gov/api/citations/20030093642/downloads/20030093642.pdf (accessed on 20 October 2024).
41. Lee, Z.; Shang, S.; Wang, Y.; Wei, J.; Ishizaka, J. Nature of optical products inverted semianalytically from remote sensing reflectance of stratified waters. *Limnol. Oceanogr.* **2020**, *65*, 387–400. [CrossRef]
42. Gilerson, A.; Herrera-Estrella, E.; Foster, R.; Agagliate, J.; Hu, C.; Ibrahim, A.; Franz, B. Determining the Primary Sources of Uncertainty in Retrieval of Marine Remote Sensing Reflectance from Satellite Ocean Color Sensors. *Front. Remote Sens.* **2022**, *3*, 857530. [CrossRef]
43. Loisel, H.; Jorge, D.S.F.; Reynolds, R.A.; Stramski, D. A synthetic optical database generated by radiative transfer simulations in support of studies in ocean optics and optical remote sensing of the global ocean. *Earth Syst. Sci. Data* **2023**, *15*, 3711–3731. [CrossRef]
44. Bi, S.; Hieronymi, M.; Röttgers, R. Bio-geo-optical modelling of natural waters. *Front. Mar. Sci.* **2023**, *10*, 1196352. [CrossRef]
45. Kolluru, S.; Gedam, S.S.; Inamdar, A.B. Subcomponent inherent optical properties retrieval from total absorption coefficient and remote sensing reflectance measured in coastal waters. *J. Earth Syst. Sci.* **2021**, *130*, 159. [CrossRef]
46. Jordan, T.M.; Dall'Olmo, G.; Tilstone, G.; Brewin, R.J.W.; Nencioli, F.; Airs, R.; Thomas, C.S.; Schlüter, L. A compilation of surface inherent optical properties and phytoplankton pigment concentrations from the Atlantic Meridional Transect. *Earth Syst. Sci. Data* **2025**, *17*, 493–516. [CrossRef]
47. Fumenia, A.; Loisel, H.; Reynolds, R.A.; Stramski, D. Relationships between the concentration of particulate organic nitrogen and the inherent optical properties of seawater in oceanic surface waters. *EGUsphere* **2024**, *2024*, 1–41.
48. Andrade, C.; Alcântara, E.; Bernardo, N.; Kampel, M. An assessment of semi-analytical models based on the absorption coefficient in retrieving the chlorophyll-a concentration from a reservoir. *Adv. Space Res.* **2019**, *63*, 2175–2188. [CrossRef]
49. Houskeeper, H.F.; Draper, D.; Kudela, R.M.; Boss, E. Chlorophyll absorption and phytoplankton size information inferred from hyperspectral particulate beam attenuation. *Appl. Opt.* **2020**, *59*, 6765. [CrossRef]

50. Wang, Y.; Liu, H.; Wu, G. Satellite retrieval of oceanic particulate organic nitrogen concentration. *Front. Mar. Sci.* **2022**, *9*, 943867. [CrossRef]
51. Koestner, D.; Stramski, D.; Reynolds, R.A. A Multivariable Empirical Algorithm for Estimating Particulate Organic Carbon Concentration in Marine Environments from Optical Backscattering and Chlorophyll-a Measurements. *Front. Mar. Sci.* **2022**, *9*, 941950. [CrossRef]
52. Stramski, D.; Joshi, I.; Reynolds, R.A. Ocean color algorithms to estimate the concentration of particulate organic carbon in surface waters of the global ocean in support of a long-term data record from multiple satellite missions. *Remote Sens. Environ.* **2022**, *269*, 112776. [CrossRef]
53. Kong, C.E.; Sathyendranath, S.; Jackson, T.; Stramski, D.; Brewin, R.J.W.; Kulk, G.; Jönsson, B.F.; Loisel, H.; Galí, M.; Le, C. Comparison of ocean-colour algorithms for particulate organic carbon in global ocean. *Front. Mar. Sci.* **2024**, *11*, 1309050. [CrossRef]
54. Galí, M.; Falls, M.; Claustre, H.; Aumont, O.; Bernardello, R. Bridging the gaps between particulate backscattering measurements and modeled particulate organic carbon in the ocean. *Biogeosciences* **2022**, *19*, 1245–1275. [CrossRef]
55. Kobayashi, H.; Toratani, M.; Matsumura, S.; Siripong, A.; Lirdwitayaprasit, T.; Jintasaeranee, P. Optical Properties of Inorganic Suspended Solids and Their Influence on Coastal Ocean Color Remote Sensing. *Int. Arch. Photogramm. Remote Sens. Spat. Inf. Sci.* **2010**, *38*, 997–1001.
56. Fuller, C.B.; Bonner, J.S.; Islam, M.S.; Ojo, T.; Page, C.A.; Kirkey, W.D. Estimating colloidal concentration using acoustic backscatter. *IEEE Sens. J.* **2013**, *13*, 4546–4555. [CrossRef]
57. Sahin, C.; Verney, R.; Sheremet, A.; Voulgaris, G. Acoustic backscatter by suspended cohesive sediments: Field observations, Seine Estuary, France. *Cont. Shelf Res.* **2017**, *134*, 39–51. [CrossRef]
58. Vergne, A.; Le Coz, J.; Berni, C. Some Backscatter Modeling Issues Complicating the Sonar-Based Monitoring of Suspended Sediments in Rivers. *Water Resour. Res.* **2023**, *59*, e2022WR032341. [CrossRef]
59. Adjovu, G.E.; Stephen, H.; James, D.; Ahmad, S. Overview of the Application of Remote Sensing in Effective Monitoring of Water Quality Parameters. *Remote Sens.* **2023**, *15*, 1938. [CrossRef]
60. Mitchell, C.; Cunningham, A.; McKee, D. Remote sensing of shelf sea optical properties: Evaluation of a quasi-analytical approach for the Irish Sea. *Remote Sens. Environ.* **2014**, *143*, 142–153. [CrossRef]
61. Mizunoya, T.; Nozaki, N.; Singh, R.K. Impact of the municipal merger on watershed management: A study of Lake Kasumigaura, Japan. *Asia-Pac. J. Reg. Sci.* **2021**, *5*, 673–704. [CrossRef]
62. Jeppesen, E.; Meerhoff, M.; Davidson, T.A.; Trolle, D.; Søndergaard, M.; Lauridsen, T.L.; Beklioglu, M.; Brucet, S.; Volta, P.; González-Bergonzoni, I.; et al. Climate change impacts on lakes: An integrated ecological perspective based on a multi-faceted approach, with special focus on shallow lakes. *J. Limnol.* **2014**, *73* (Suppl. 1), 88–111.
63. Oyama, Y.; Matsushita, B.; Fukushima, T.; Nagai, T.; Imai, A. A new algorithm for estimating chlorophyll-a concentration from multi-spectral satellite data in case II waters: A simulation based on a controlled laboratory experiment. *Int. J. Remote Sens.* **2007**, *28*, 1437–1453. [CrossRef]
64. Oyama, Y.; Matsushita, B.; Fukushima, T.; Matsushige, K.; Imai, A. Application of spectral decomposition algorithm for mapping water quality in a turbid lake (Lake Kasumigaura, Japan) from Landsat TM data. *ISPRS J. Photogramm. Remote Sens.* **2009**, *64*, 73–85. [CrossRef]
65. Oyama, Y.; Matsushita, B.; Fukushima, T.; Chen, J.; Nagai, T.; Imai, A. Testing the spectral decomposition algorithm (SDA) for different phytoplankton species by a simulation based on tank experiments. *Int. J. Remote Sens.* **2010**, *31*, 1605–1623. [CrossRef]
66. Nguyen, T.N.; Kasuga, I.; Liu, M.; Katayama, H. Occurrence of antibiotic resistance genes as emerging contaminants in watersheds of Tama River and Lake Kasumigaura in Japan. In *IOP Conference Series: Earth and Environmental Science*; Institute of Physics Publishing: Bristol, UK, 2019; Volume 266.
67. Higano, Y.; Sawada, T. The Dynamic Optimal Policy to Improve the Water Quality of Lake Kasumigaura. *Stud. Reg. Sci.* **1996**, *26*, 75–86. [CrossRef]
68. Takamura, N.; Nakagawa, M. Photosynthesis and primary production in Lake Kasumigaura (Japan) monitored monthly since 1981. *Ecol. Res.* **2016**, *31*, 287. [CrossRef]
69. Fukushima, T.; Arai, H. Regime shifts observed in Lake Kasumigaura, a large shallow lake in Japan: Analysis of a 40-year limnological record. *Lakes Reserv. Sci. Policy Manag. Sustain. Use* **2015**, *20*, 54–68. [CrossRef]
70. MOE. MOE. 2023. Available online: https://www.env.go.jp/en/water/wq/lakes/origin.html (accessed on 1 July 2024).
71. Lubac, B.; Loisel, H. Variability and classification of remote sensing reflectance spectra in the eastern English Channel and southern North Sea. *Remote Sens. Environ.* **2007**, *110*, 45–58. [CrossRef]
72. Higa, H.; Ideno, R.; Salem, S.I.; Kobayashi, H. Uncertainty Analysis of Particle Backscattering Coefficient Measurement for Multiple Highly Turbid Water Areas in Ocean Color Remote Sensing. *Sens. Mater.* **2023**, *35*, 3807–3828. [CrossRef]
73. HOBI Labs. HydroScat-6P Spectral Backscattering Sensor & Fluorometer User's Manual. 2010. Available online: www.hobilabs.com (accessed on 25 October 2023).

74. Babin, B.J.; Hardesty, D.M.; Suter, T.A. Color and shopping intentions: The intervening effect of price fairness and perceived affect. *J. Bus. Res.* **2003**, *56*, 541–551. [CrossRef]
75. Neeley, A.R.; Mannino, A. (Eds.) *IOCCG Protocol Series Ocean Optics & Biogeochemistry Protocols for Satellite Ocean Colour Sensor Validation Volume 1: Inherent Optical Property Measurements and Protocols: Absorption Coefficient*; IOCCG Protocol Series; IOCCG: Dartmouth, NS, Canada, 2018.
76. Kishino, M.; Takahashi, M.; Okami, N.; Ichimura, S. Estimation of the Spectral Absorption Coefficients of Phytoplankton In The Sea. *Bull. Mar. Sci.* **1985**, *37*, 634–642.
77. Sosik, H.M.; Mitchell, B.G. Absorption, fluorescence, and quantum yield for growth in nitrogen-limited Dunaliella tertiolecta. *Limnol. Oceanogr.* **1991**, *36*, 910–921. [CrossRef]
78. Yamashita, Y. Algorithm Description Ver. 1 (Vol. 1). Japan Aerospace Exploration Agency (JAXA). 2016. Available online: https://suzaku.eorc.jaxa.jp/GCOM_C/data/ATBD/ver2/V2ATBD_O3AB_CDOMa_Hirata.pdf (accessed on 25 February 2024).
79. National Institute for Environmental Studies. Lake Kasumigaura Database, National Institute for Environmental Studies, Japan. 2016. Available online: https://db.cger.nies.go.jp/gem/moni-e/inter/GEMS/database/kasumi/contents/intro.html (accessed on 30 June 2024).
80. Takamura, N.; Nakagawa, M.; Hanazato, T. Zooplankton abundance in the pelagic region of Lake Kasumigaura (Japan): Monthly data since 1980. *Ecol. Res.* **2017**, *32*. [CrossRef]
81. National Institute for Environmental Studies. Lake Kasumigaura Database Interpretations of Observed Data. 2012. Available online: http://db.cger.nies.go.jp/gem/moni-e/inter/GEMS/database/kasumi/contents/database/datalist.html (accessed on 20 January 2024).
82. Alvado, B.; Sòria-Perpinyà, X.; Vicente, E.; Delegido, J.; Urrego, P.; Ruíz-Verdú, A.; Soria, J.M.; Moreno, J. Estimating organic and inorganic part of suspended solids from sentinel 2 in different inland waters. *Water* **2021**, *13*, 2453. [CrossRef]
83. Schartau, M.; Riethmüller, R.; Flöser, G.; van Beusekom, J.E.E.; Krasemann, H.; Hofmeister, R.; Wirtz, K. On the separation between inorganic and organic fractions of suspended matter in a marine coastal environment. *Prog. Oceanogr.* **2019**, *171*, 231–250. [CrossRef]
84. Redfield, A.C. On the Proportions of Organic Derivatives in Sea Water and Their Relation to the Composition of Plankton. 1934. Available online: https://www.researchgate.net/publication/344709447 (accessed on 12 June 2024).
85. Redfield, A.C. The biological control of chemical factors in the environment. *Am. Sci.* **1958**, *46*, 230A-221.
86. Pinet, S.; Martinez, J.-M.; Ouillon, S.; Lartiges, B.; Villar, R.E. Variability of apparent and inherent optical properties of sediment-laden waters in large river basins–lessons from in situ measurements and bio-optical modeling. *Opt. Express* **2017**, *25*, A283. [CrossRef] [PubMed]
87. Hoge, F.E.; Lyon, P.E.; Mobley, C.D.; Sundman, L.K. Radiative transfer equation inversion: Theory and shape factor models for retrieval of oceanic inherent optical properties. *J. Geophys. Res. Ocean.* **2003**, *108*. [CrossRef]
88. Mobley, C. Remote-Sensing Retrieval of Oceanic Inherent Optical Properties by Inversion of the Radiative Transfer Equation. 2002. Available online: https://www.researchgate.net/publication/235033012 (accessed on 25 January 2024).
89. Toratani, M.; Ogata, K.; Fukushima, H. SGLI Algorithm Theoretical Basis Document Atmospheric Correction Algorithm for Ocean Color. 2021. Available online: https://suzaku.eorc.jaxa.jp/GCOM_C/data/ATBD/ver3/V3ATBD_O2AB_NWLR_toratani.pdf (accessed on 24 July 2023).
90. Gordon, H.R.; Wang, M. Retrieval of water-leaving radiance and aerosol optical thickness over the oceans with SeaWiFS: A preliminary algorithm. *Appl. Opt.* **1994**, *33*, 443–452. [CrossRef]
91. Fukushima', H.; Toratani', M.; Yamamiya', S.; Mitom, Y. Atmospheric correction algorithms for adeos/octs ocean color data: Performance comparison based on ship and buoy measurements. *Adv. Space Res.* **2000**, *25*, 1015–1024. [CrossRef]
92. Fukushima, H.; Toratani, M.; Murakami, H.; Deschamps, P.Y.; Frouin, R.; Tanaka, A. Evaluation of ADEOS-II GLI ocean color atmospheric correction using SIMBADA handheld radiometer data. *J. Oceanogr.* **2007**, *63*, 533–543. [CrossRef]
93. Salem, S.I.; Toratani, M.; Higa, H.; Son, S.H.; Siswanto, E.; Ishizaka, J. Long-Term Evaluation of GCOM-C/SGLI Reflectance and Water Quality Products: Variability Among JAXA G-Portal and JASMES. *Remote Sens.* **2025**, *17*, 221. [CrossRef]
94. Bailey, S.; He, X.; Jamet, C.; Ruddick, K.; Shanmugam, P.; Schroeder, T.; Stamnes, K.; Sterckx, S.; Steinmetz, F. IOCCG Technical Series Evaluation of Atmospheric Correction Algorithms over Turbid Waters Editors: Cédric Jamet Authors. 2019. Available online: https://ioccg.org/wp-content/uploads/2019/12/ioccg_atm-corr-report21nov2019.pdf (accessed on 28 June 2024).
95. Gordon, H.R. A semianalytic radiance model of ocean color. *J. Geophys. Res.* **1988**, *93*, 10909–10924. [CrossRef]
96. Hoge, F.E.; Wright, C.W.; Lyon, P.E.; Swift, R.N.; Yungel, J.K. Inherent optical properties imagery of the western North Atlantic Ocean: Horizontal spatial variability of the upper mixed layer. *J. Geophys. Res. Ocean.* **2001**, *106*, 31129–31140. [CrossRef]
97. Lyon, P.E.; Hoge, F.E.; Wright, C.W.; Swift, R.N.; Yungel, J.K. Chlorophyll biomass in the global oceans: Satellite retrieval using inherent optical properties. *Appl. Opt.* **2004**, *43*, 5886–5892. [CrossRef]

98. Werdell, P.J.; McKinna, L.I.; Boss, E.; Ackleson, S.G.; Craig, S.E.; Gregg, W.W.; Lee, Z.; Maritorena, S.; Roesler, C.S.; Rousseaux, C.S.; et al. An overview of approaches and challenges for retrieving marine inherent optical properties from ocean color remote sensing. *Prog. Oceanogr.* **2018**, *160*, 186–212. [CrossRef] [PubMed]
99. Wang, J.; Wang, Y.; Lee, Z.; Wang, D.; Chen, S.; Lai, W. A revision of NASA SeaDAS atmospheric correction algorithm over turbid waters with artificial Neural Networks estimated remote-sensing reflectance in the near-infrared. *ISPRS J. Photogramm. Remote. Sens.* **2022**, *194*, 235–249. [CrossRef]
100. Liu, X.; Yang, Q.; Wang, Y.; Zhang, Y. Evaluation of GOCI Remote Sensing Reflectance Spectral Quality Based on a Quality Assurance Score System in the Bohai Sea. *Remote Sens.* **2022**, *14*, 1075. [CrossRef]
101. Guan, X.; Liu, Y. Bayesian Analysis for Fatigue Damage Prognostics and Remaining Useful Life Prediction. In *Machine Learning and Knowledge Discovery for Engineering Systems Health Management*; Chapman and Hall/CRC: Boca Raton, FL, USA, 2012; pp. 203–243.
102. Hodson, T.O. Root mean square error (RMSE) or mean absolute error (MAE): When to use them or not. *Geosci. Model Dev.* **2022**, *15*, 5481–5487. [CrossRef]
103. Słomska-Przech, K.; Panecki, T.; Pokojski, W. Heat maps: Perfect maps for quick reading? comparing usability of heat maps with different levels of generalization. *ISPRS Int. J. Geo-Inf.* **2021**, *10*, 562. [CrossRef]
104. Simão, M.L.; Videiro, P.M.; Silva, P.B.A.; de Freitas Assad, L.P.; Sagrilo, L.V.S. Application of Taylor diagram in the evaluation of joint environmental distributions' performances. *Mar. Syst. Ocean Technol.* **2020**, *15*, 151–159. [CrossRef]
105. Taylor, K.E. Summarizing multiple aspects of model performance in a single diagram. *J. Geophys. Res. Atmos.* **2001**, *106*, 7183–7192. [CrossRef]
106. Salem, S.I.; Higa, H.; Kim, H.; Kazuhiro, K.; Kobayashi, H.; Oki, K.; Oki, T. Multi-algorithm indices and look-up table for chlorophyll-a retrieval in highly turbid water bodies using multispectral data. *Remote Sens.* **2017**, *9*, 556. [CrossRef]
107. O'Shea, R.E.; Pahlevan, N.; Smith, B.; Boss, E.; Gurlin, D.; Alikas, K.; Kangro, K.; Kudela, R.M.; Vaičiūtė, D. A hyperspectral inversion framework for estimating absorbing inherent optical properties and biogeochemical parameters in inland and coastal waters. *Remote Sens. Environ.* **2023**, *295*, 113706. [CrossRef]
108. Bricaud, A.; Morel, A.; Babin, M.; Allali, K.; Claustre, H. Variations of light absorption by suspended particles with chlorophyll a concentration in oceanic (case 1) waters: Analysis and implications for bio-optical models. *J. Geophys. Research. Ocean.* **1998**, *103*, 33–64. [CrossRef]
109. Rasse, R.; Dall'Olmo, G.; Graff, J.; Westberry, T.K.; van Dongen-Vogels, V.; Behrenfeld, M.J. Evaluating optical proxies of particulate organic carbon across the surface Atlantic ocean. *Front. Mar. Sci.* **2017**, *4*, 367. [CrossRef]
110. Huang, C.; Jiang, Q.; Yao, L.; Yang, H.; Lin, C.; Huang, T.; Zhang, Y. Variation pattern of particulate organic carbon and nitrogen in oceans and inland waters. *Biogeosciences* **2018**, *15*, 1827–1841. [CrossRef]
111. Schindler Wildhaber, Y.; Liechti, R.; Alewell, C. Organic matter dynamics and stable isotope signature as tracers of the sources of suspended sediment. *Biogeosciences* **2012**, *9*, 1985–1996. [CrossRef]
112. Spencer, R.G.M.; Butler, K.D.; Aiken, G.R. Dissolved organic carbon and chromophoric dissolved organic matter properties of rivers in the USA. *J. Geophys. Res. Biogeosci.* **2012**, *117*. [CrossRef]
113. Dadolahi, S.A.; Mohammad, A.H. Assessment of chromophoric dissolved organic matter and nutrient distribution in New Zealand rivers using satellite images. *Appl. Ecol. Environ. Res.* **2019**, *17*, 3575–3589. [CrossRef]
114. Isada, T.; Abe, H.; Kasai, H.; Nakaoka, M. Dynamics of Nutrients and Colored Dissolved Organic Matter Absorption in a Wetland-Influenced Subarctic Coastal Region of Northeastern Japan: Contributions from Mariculture and Eelgrass Meadows. *Front. Mar. Sci.* **2021**, *8*, 711832. [CrossRef]
115. Kobayashi, S.; Nakada, S.; Nakajima, M.; Yamamoto, K.; Akiyama, S.; Fuchi, M.; Hayashi, M.; Ishizaka, J. Visualization of the distribution of dissolved organic matter in Osaka Bay using a satellite ocean color sensor (COMS/GOCI). *J. Water Environ. Technol.* **2017**, *15*, 55–64. [CrossRef]
116. Koliyavu, T.; Martias, C.; Singh, A.; Mounier, S.; Gérard, P.; Dupouy, C. Situ Variability of DOM in Relation with Biogeochemical and Physical Parameters in December 2017 in Laucala Bay (Fiji Islands) after a Strong Rain Event. *J. Mar. Sci. Eng.* **2021**, *2021*, 241. [CrossRef]
117. Arellano, A.R.; Coble, P.G. Assessing carbon and nutrient inputs in a spring-fed estuary using fluorescence spectroscopy and discriminatory classification. *Limnol. Oceanogr.* **2015**, *60*, 789–804. [CrossRef]
118. Doxaran, D.; Ehn, J.; Bélanger, S.; Matsuoka, A.; Hooker, S.; Babin, M. Optical characterisation of suspended particles in the Mackenzie River plume (Canadian Arctic Ocean) and implications for ocean colour remote sensing. *Biogeosciences* **2012**, *9*, 3213–3229. [CrossRef]
119. Martinez-Vicente, V.; Land, P.E.; Tilstone, G.H.; Widdicombe, C.; Fishwick, J.R. Particulate scattering and backscattering related to water constituents and seasonal changes in the Western English Channel. *J. Plankton Res.* **2010**, *32*, 603–619. [CrossRef]
120. Favareto, L.R.; Rudorff, N.; Kampel, M.; Frouin, R.; Röttgers, R.; Doxaran, D.; Murakami, H.; Dupouy, C. Bio-optical characterization and ocean colour inversion in the Eastern Lagoon of New Caledonia, South Tropical Pacific. *Remote Sens.* **2018**, *10*, 1043. [CrossRef]

121. Ishizaka, J.; Yang, M.; Fujii, N.; Katano, T.; Hori, M.; Mine, T.; Saitoh, K.; Murakami, H. Use of AERONET-OC for validation of SGLI/GCOM-C products in Ariake Sea, Japan. *J. Oceanogr.* **2022**, *78*, 291–309. [CrossRef]
122. Terrel, M.M.; Fukushima, T.; Matsushita, B.; Yoshimura, K.; Imai, A. Long-term light environment variability in Lake Biwa and Lake Kasumigaura, Japan: Modeling approach. *Limnology* **2012**, *13*, 237–252. [CrossRef]
123. Miyazaki, T. Measuring the Water Quality of Lake Kasumigaura by LANDSAT. Remote Sensing. 1986. Available online: https://www.nies.go.jp/kanko/kenkyu/pdf/972089-1.pdf (accessed on 3 March 2024).
124. Jaelani, L.M.; Matsushita, B.; Yang, W.; Fukushima, T. Evaluation of four MERIS atmospheric correction algorithms in Lake Kasumigaura, Japan. *Int. J. Remote Sens.* **2013**, *34*, 8967–8985. [CrossRef]
125. Ogashawara, I.; Mishra, D.R.; Nascimento, R.F.F.; Alcântara, E.H.; Kampel, M.; Stech, J.L. Re-parameterization of a quasi-analytical algorithm for colored dissolved organic matter dominant inland waters. *Int. J. Appl. Earth Obs. Geoinf.* **2016**, *53*, 128–145. [CrossRef]
126. Grunert, B.K.; Mouw, C.B.; Ciochetto, A.B. Deriving inherent optical properties from decomposition of hyperspectral non-water absorption. *Remote Sens. Environ.* **2019**, *225*, 193–206. [CrossRef]
127. Kritten, L.; Preusker, R.; Brockmann, C.; Fincke, T.; Koponen, S.; Fischer, J. Water remote sensing reflectance from radiative transfer simulations on a global scale of Inherent Optical Properties. *Earth Syst. Sci. Data Discuss.* **2018**, *2018*, 1–14.
128. Hu, C.; Lee, Z.; Franz, B. Chlorophyll a algorithms for oligotrophic oceans: A novel approach based on three-band reflectance difference. *J. Geophys. Res. Ocean.* **2012**, *117*, C01011. [CrossRef]
129. Watanabe, F.; Mishra, D.R.; Astuti, I.; Rodrigues, T.; Alcântara, E.; Imai, N.N.; Barbosa, C. Parametrization and calibration of a quasi-analytical algorithm for tropical eutrophic waters. *ISPRS J. Photogramm. Remote Sens.* **2016**, *121*, 28–47. [CrossRef]
130. Lewis, K.M.; Arrigo, K.R. Ocean Color Algorithms for Estimating Chlorophyll a, CDOM Absorption, and Particle Backscattering in the Arctic Ocean. *J. Geophys. Res. Ocean.* **2020**, *125*, e2019JC015706. [CrossRef]
131. Woźniak, S.B.; Stramski, D.; Stramska, M.; Reynolds, R.A.; Wright, V.M.; Miksic, E.Y.; Cichocka, M.; Cieplak, A.M. Optical variability of seawater in relation to particle concentration, composition, and size distribution in the nearshore marine environment at Imperial Beach, California. *J. Geophys. Res. Ocean.* **2010**, *115*. [CrossRef]
132. Stramski, D.; Bricaud, A.; Morel, A. Modeling the inherent optical properties of the ocean based on the detailed composition of the planktonic community. *Appl. Opt.* **2001**, *40*, 2929. [CrossRef] [PubMed]
133. Twardowski, M.S.; Boss, E.; Macdonald, J.B.; Pegau, W.S.; Barnard, A.H.; Zaneveld, J.R.V. A model for estimating bulk refractive index from the optical backscattering ratio and the implications for understanding particle composition in case I and case II waters. *J. Geophys. Res. Ocean.* **2001**, *106*, 14129–14142. [CrossRef]
134. Cunningham, A.; Ramage, L.; McKee, D. Relationships between inherent optical properties and the depth of penetration of solar radiation in optically complex coastal waters. *J. Geophys. Res. Ocean.* **2013**, *118*, 2310–2317. [CrossRef]
135. Xue, K.; Ma, R.; Duan, H.; Shen, M.; Boss, E.; Cao, Z. Inversion of inherent optical properties in optically complex waters using sentinel-3A/OLCI images: A case study using China's three largest freshwater lakes. *Remote Sens. Environ.* **2019**, *225*, 328–346. [CrossRef]
136. Tripathy, S.C.; Kerkar, A.U.; Sabu, P.; Padhi, S.K.; Pandi, S.R.; Sarkar, A.; Parli, B.V.; Mohan, R. Short-term time-series observations of phytoplankton light-absorption and productivity in Prydz Bay, coastal Antarctica. *Front. Mar. Sci.* **2024**, *11*, 1420179. [CrossRef]
137. Wei, J.; Wang, M.; Mikelsons, K.; Jiang, L. Chlorophyll-Specific Absorption Coefficient of Phytoplankton in World Oceans: Seasonal and Regional Variability. *Remote Sens.* **2023**, *15*, 2423. [CrossRef]
138. Murakami, H. Algorithm Theoretical Basis Document (ATBD) of GCOM-C Chlorophyll-a Concentration Algorithm (Version 2). Japan Aerospace Exploration Agency (JAXA). 2018. Available online: https://suzaku.eorc.jaxa.jp/GCOM_C/data/ATBD/ver2/V2ATBD_O3AB_Chla_Murakami.pdf (accessed on 10 May 2024).
139. Bricaud, A.; Babin, M.; Morel, A.; Claustre, H. Variability in the chlorophyll-specific absorption coefficients of natural phytoplankton: Analysis and parameterization. *J. Geophys. Res.* **1995**, *100*, 13321–13332. [CrossRef]
140. Lee, Z.; Shang, S.; Hu, C.; Lewis, M.; Arnone, R.; Li, Y.; Lubac, B. Time series of bio-optical properties in a subtropical gyre: Implications for the evaluation of interannual trends of biogeochemical properties. *J. Geophys. Res. Ocean.* **2010**, *115*. [CrossRef]
141. Duan, H.; Ma, R.; Simis, S.; Zhang, Y. Validation of MERIS case-2 water products in lake taihu, China. *GIScience Remote Sens.* **2012**, *49*, 873–894. [CrossRef]
142. Blondeau-Patissier, D.; Schroeder, T.; Clementson, L.A.; Brando, V.E.; Purcell, D.; Ford, P.; Williams, D.K.; Doxaran, D.; Anstee, J.; Thapar, N.; et al. Bio-optical properties of two neigboring coastal regions of tropical Northern Australia: The Van Diemen Gulf and Darwin Harbour. *Front. Mar. Sci.* **2017**, *4*, 114. [CrossRef]

Disclaimer/Publisher's Note: The statements, opinions and data contained in all publications are solely those of the individual author(s) and contributor(s) and not of MDPI and/or the editor(s). MDPI and/or the editor(s) disclaim responsibility for any injury to people or property resulting from any ideas, methods, instructions or products referred to in the content.